



Accepted Article

Self entrainment motion of a slow-moving landslide inferred from Landsat-8 time-series

Pascal Lacroix¹, Gael Araujo², James Hollingsworth¹, and Edu Taipe²

¹ISTerre - IRD/CNRS/Universite de Grenoble / 1381, rue de la piscine / 38400 Saint Martin d'Heres,

France

²INGEMMET, Urb. Las Begonias B-3 / Jose Luis Bustamante y Rivero / Arequipa, Peru

Key Points:

- Landsat-8 images are used to measure a 5.7 years long time-series of displacement over a slow-moving landslide
- A seasonal artifact in the Landsat-8 images caused by illumination effects in steep topography is identified and corrected
- A retrogression of the landslide headscarp generates tilting and acceleration of the downward landslide mass

This article has been accepted for publication and undergone full peer review but has not been through the copyediting, typesetting, pagination and proofreading process which may lead to differences between this version and the Version of Record. Please cite this article as doi: 10.1029/2018JF004920

Corresponding author: Pascal Lacroix, pascal.lacroix@univ-grenoble-alpes.fr

Abstract

In mountainous environments, slow-moving landslides (velocities <100 m/yr) are a major concern for local populations. Rainfall is often the dominant forcing, and often result in major changes in kinematics which can mask smaller signals related to internal forcings. We focus here on a major (> 40 Mm³) slow-moving landslide in the desert of southern Peru, and take advantage of this arid environment to study the internal processes affecting landslide kinematics. We first estimate the ground displacement from time-series analysis of Landsat-8 images, spanning a 5.7 year period. Systematic artifacts in the optical time-series are shown to correlate with topography, as well as vary seasonally. We apply a novel procedure for correcting these artifacts, which significantly reduces noise in the resulting time-series, thereby allowing us to precisely resolve landslide displacements. We find landslide velocities of up to 35 m/yr, with complex non-linear inter-annual pattern, including a period of rapid acceleration. We validate our optically-derived time-series using GNSS field measurements, and find uncertainties (RMSE) on the moving mass of 1.12 to 1.55 m. Sudden acceleration of the landslide body after March 2016 may originate from a mass collapse due to retrogression of the headscarp. By coupling sparse 3D GNSS measurements with dense 2D optical time-series data, we show that the headscarp retrogression acts like a wedge, resulting in domino-like tilting of the downward blocks, and accelerates basal sliding over two years. These observations reveal that the dynamics of this retrogressive landslide are predominantly controlled by sediment supply, and that succession of retrogressive and advancing motions is a self entrainment process.

1 Introduction

Slow-moving landslides (< 100 m/yr (Cruden & Varnes, 1996)) pose a major ongoing threat for local populations, preventing agricultural irrigation, damaging roads and infrastructure. These landslides show a large diversity in kinematics (e.g. periods of quiescence and acceleration), and can sometimes evolve toward catastrophic failure (Hendron & Patton, 1985). Many examples reveal that most catastrophic landslides are preceded by a phase of creep, characteristic of slow-moving landslides (Federico et al., 2012). As a consequence the study of slow-moving landslides may lead a better understanding of the physical processes governing both slow and rapid landslides (Palmer, 2017). In recent years, various studies of slow-moving landslides (e.g. Iverson & Major, 1987; Reid, 1994; Schulz et al., 2009; Handwerger et al., 2013; Hsu et al., 2014; Lacroix et al., 2014; Handwerger et al., 2015; Lacroix et al., 2015; Bennett et al., 2016; Zerathe et al., 2016) have revealed a rich diversity in kinematics, with various forcing factors, e.g. rainfall, earthquakes, glacial retreat, and anthropogenic activity. These forcings act over a wide variety of time-scales, from seconds (earthquakes (Lacroix et al., 2014)), to several decades (glacial retreat (Strozzi et al., 2010)), thus making their study challenging.

Landslide motion is often interpreted to occur as a direct consequence of external forcing factors (e.g. Reid, 1994; Handwerger et al., 2013; Hsu et al., 2014; Lacroix et al., 2014; Handwerger et al., 2015; Zerathe et al., 2016), such as rainfall or ground shaking (i.e. from earthquakes). However, different internal processes may also influence landslide motion; e.g. progressive failure is thought play a key role in the initiation of landslide motion (Amitrano, 2004; Eberhardt et al., 2004; Lacroix & Amitrano, 2013; Carey & Petley, 2014; Gischig et al., 2016). Redistribution of mass within a moving landslide can also continuously modify the stress field, leading to complex variations in landslide motion (Booth et al., 2018); e.g. destabilization of the headscarp at the rear of the landslide can occur by removal of the lateral confining pressure, in turn leading to landslide development by retrogression of its headscarp (e.g. Locat et al., 2011). Some studies also highlight that in clay-rich sediments, debris coming from outside the landslide can lead to destabilization through the generation of dynamic perturbations of already high pore pressures (in undrained conditions, e.g. Iverson & LaHusen, 1989; Booth et al., 2018)

— this effect is well-known for sub-marine landslides (e.g. Mountjoy et al., 2009; Urgeles & Camerlenghi, 2013). However, few previous studies have investigated the effect of retrogressive motions on the advancing body mass for stiffer materials typical of terrestrial landslides. To address this issue, we focus our study on the in-situ observation and analysis of a slow moving landslide in southern Peru.

Studying the internal processes leading to landslide development through in-situ observations is limited by two factors. First, the internal processes can last for many years, making them challenging to measure (e.g. Lacroix & Amitrano, 2013). Second, the landslide dynamics are often affected by external factors, particularly precipitation (e.g. Iverson, 2000), which can mask any subtle signals related to internal processes. Studying active landslides in arid regions, where rainfall plays a limited role on landslide development, can help to isolate the contribution made by internal processes on the dynamics of landslides. Slow-moving landslides are somewhat understudied in desert regions, in part due to the low population densities, and consequently low impact of these landslides on local populations. We focus here on a very-large ($>40 \text{ Mm}^3$) slow-moving landslide (Siguas) in southern Peru, in one of the driest areas on Earth. This landslide was previously reported by Hermanns et al. (2012), who attributed its initiation to vast irrigation programs. In this study, we take advantage of the limited natural external forcings (i.e. precipitation) and the known anthropogenic forcing (irrigation) acting on this landslide, to study the internal processes involved in its recent development.

We base our analysis of the Siguas landslide on the detailed monitoring of its kinematics. Landslide kinematics can be estimated using different approaches, e.g. using ground-based GNSS monitoring, or remote sensing-based methods, i.e. radar (e.g. Hilley et al., 2004; Calabro et al., 2010) or optical images (e.g. Delacourt et al., 2004; Stumpf et al., 2014; Lacroix et al., 2015). For landslide studies, optical images have the advantage of a close to nadir (i.e.. vertical incidence) viewing geometry, allowing geomorphic processes to be monitored on steep slopes. Furthermore, correlation of optical imagery is less sensitive than InSAR to decorrelation resulting from large motions, or from long time periods between image acquisitions. Landslide motion can be inferred by the correlation of multiple-date optical images, leading to a time-series of ground motions which reveal the spatial evolution of the landslide, with uncertainties of between $1/8^{\text{th}}$ and half of a pixel, depending on the sensor (e.g. Stumpf et al., 2014). The recent development of time-series analysis in optical image correlation takes advantage of the redundancy of data to provide robust displacement time-series; uncertainties can be reduced by more than 30% compared with pair-wise time-series analysis when using medium resolution SPOT1-5 satellites over time-periods of ~ 30 years (Bontemps et al., 2018). The use of modern medium-resolution satellite data, such as Sentinel-2 or Landsat-7/8 images (with high temporal sampling every 5 and 8 days at the equator, respectively) has also been used in a pairwise processing to derive time-series of ground surface displacement (e.g. Dehecq et al., 2015; Fahnestock et al., 2015; Lacroix et al., 2018). However, exploitation of the full data redundancy to generate robust optical time-series has been little utilized for modern multi-temporal optical satellite datasets. Recently, Altena et al. (2018) made use of a similar time-series inversion approach to Bontemps et al. (2018), to study ground deformation of glaciers using Landsat8 imagery. In this study, we develop robust time-series using Landsat8 data to derive spatio-temporal kinematic variations of a slow-moving landslide.

The rapid re-visit interval of Landsat8 should present a promising opportunity for monitoring landslides, either for detecting transient motions that may constitute precursors to rapid landslides (Lacroix et al., 2018), or for studying seasonal and longer-term landslide behaviour.

Uncertainties in landslide motion obtained with Landsat-7/8 and Sentinel-2 satellites are not well documented. Two previous estimations on stable areas using Sentinel-2 data shows a standard deviation of $\sim 1.5 \text{ m}$ in France (Lacroix et al., 2018) and between

2.6 to 3.8 m in Greenland (Kaab et al., 2016). However, these values are not necessarily representative of the motion uncertainty everywhere in the image, especially for a small and heterogeneous moving mass, such as a landslide, or glacier. Indeed, a previous study using Landsat-7 correlation data, (Dehecq et al., 2015) showed that uncertainties on moving glaciers are two times greater than in stable areas. In the context of growing interest for high-frequency optical satellite data (which offer frequent, medium (10–15 m) resolution, global sampling with open data access), there is a strong need to validate the ground motion measurements that can be obtained with such datasets.

In this study we aim both at (1) validating the use of Landsat-8 optical time-series for measuring landslide kinematics, and (2) studying the internal processes that impact landslide development. We first compute time-series of landslide motion over a period of 5.7 years using Landsat-8 data, which we then validate by comparison with GNSS campaign data. We finally study the inter-annual and transient variability in kinematics. This analysis highlights the relation between the landslide main scarp retrogression and the advancing landslide body.

2 Regional Settings

The Siguas landslide is located in southern Peru (-16.368°N 72.128°W), at an elevation of ~ 1300 m, within a vast alluvial plateau incised by a 150 m deep narrow valley dating from the Pleistocene (Figure 1). The material is formed by sediments from the Moquegua Formation (Cenozoic), and alluvial quaternary deposits made up of Pleistocene conglomerates interbedded with sands and ignimbrites. The area is one of the driest deserts on Earth, with very little precipitation (the nearby automatic weather stations from NOAA situated in Ilo and Nazca, in the same climatic context as Siguas valley, show mean annual precipitations of 0.8 and 0.04 cm/yr, respectively, for the 2013–2018 period). Vast irrigation programs, starting in 1981, resulted in water infiltration on the valley walls. This infiltration activated different mega landslides (about 40 Mm^3 (Hermanns et al., 2012)) including the Siguas landslide (Figure 2). The first signs of slope failure were documented in 2004 (Araujo, 2017), where the lower part of the slope revealed cracks, secondary small scarps, and water infiltration from irrigation as a consequence of saturation of the weak slope sediments. The landslide developed rapidly after 2004 through a retrogressive motion of its headscarp, which is now affecting various infrastructures at its crown. The headscarp is now located (Figure 1): (1) 6 m from a major irrigation canal, which was consequently abandoned in the first months of 2017, (2) ~ 50 m from the panamerican road — the main peruvian north-south communication way, and (3) ~ 75 m from a milk factory that produces 40% of the total peruvian national supply. Irrigation volumes vary slightly over the 2013–2018 period with an annual mean between 9.3 and $11.3 \text{ m}^3/\text{s}$, varying seasonally between 7 and $13.7 \text{ m}^3/\text{s}$ (Figure 3).

Due to the potential impact of the Siguas landslide to the region, precise monitoring began in 2015 with campaign GNSS (see section 3.3). A technical report (Araujo, 2017) concluded on different mitigation work that must be undertaken at short, middle and long-term periods. This includes deviation of the canal and the panamerican road, and installation of vertical wells (225 m deep) to drain the infiltrated water.

3 Data and Methods

3.1 Landsat-8 optical satellite data and processing

We obtained 51 Landsat-8 panchromatic images (15 m resolution) covering the Siguas region from the USGS EarthExplorer website. Each image was acquired on the same orbital track with a nadir view-geometry, and cropped to cover the same region of $12 \times 9 \text{ km}^2$ centered on the Siguas landslide. The sequence of images spans 5.7 years, beginning in

Accepted Article

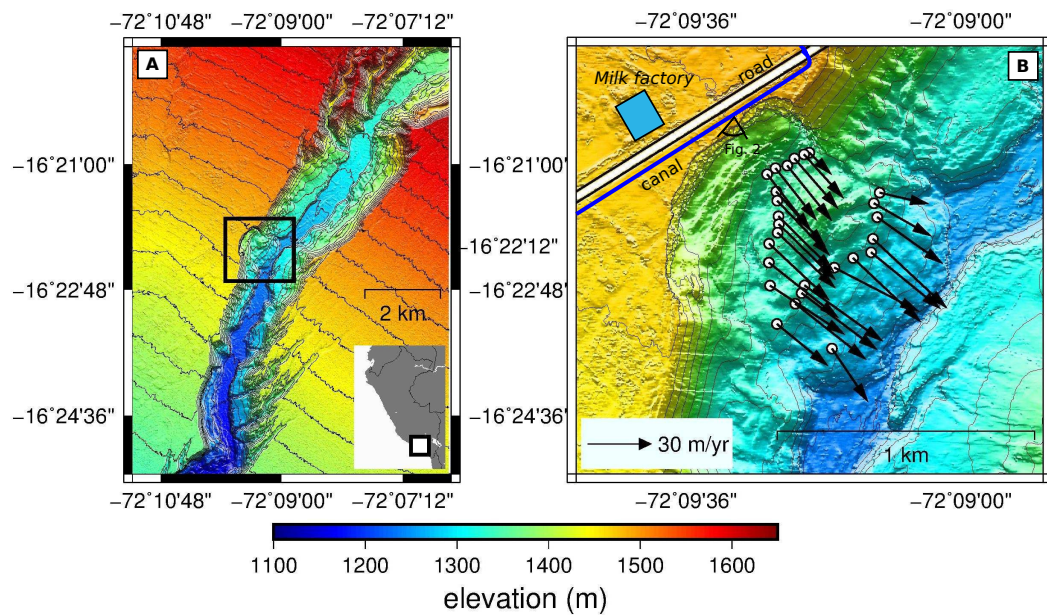


Figure 1. (a) General digital elevation model of the study area, and (b) zoom over the Siguas landslide. White circles indicate the GNSS markers, and arrows show the displacement vectors calculated over 1.5 years of GNSS campaigns (2015/11/22-2017/05/22). The white stripe shows the Panamerican road. The blue line shows the canal. The blue square shows the location of the milk factory. View direction for Figure 2 is shown. The altitude contours are spaced every 20 m.



Figure 2. Picture of the Siguas landslide head scarp from 17 April 2016, looking down toward the landslide toe. Position of the camera view is shown in Figure 1b.

March 2013 and ending in December 2018 (see SI). The images are delivered as an orthorectified product (i.e. resampled to remove topographic effects from the images), which are all aligned to a common grid.

To retrieve a displacement time-series from the available Landsat-8 imagery, we follow the correlation and inversion methodology described by Bontemps et al. (2018). We first correlate all possible image combinations (within a one year period), before removing any global mis-registration errors, and striping artifacts from mis-alignment of the CCD arrays on the Landsat-8 sensor (e.g. Leprince et al., 2008), before inverting the redundant system to provide a robust and unbiased time-series.

Each image pair was correlated in the frequency domain from the phase shift in low-frequency content within a multi-scale sliding window (64 by 32 pixels) using the COSI-Corr software package (Leprince et al., 2007). The correlation window sizes were chosen to (1) maximize the correlation potential between the two images (i.e. large windows), (2) maximize the spatial detail in resolved ground motion (i.e. small windows), (3) minimize correlation bias associated with very small windows, which can clip the low-frequency content, and (4) minimize the difference with GNSS campaign displacements (see section 3.3). Each correlation consists of a spatial map of EW and NS ground displacements (corresponding to pixel shifts in column and row), as well as correlation score which is updated in an iterative way to remove outliers (see Leprince et al., 2007); points with correlation scores below 0.7 were discarded. The correlation processing yields 608 separate displacement maps spanning 37 time-steps only. This redundant system of displacements is inverted pixelwise to estimate the displacement on the 37 different time periods (Bontemps et al., 2018). Each displacement field is weighted as a function of the time difference (Δt) between the two images of the pair to take into account for increasing decorrelation (and associated noise) with time; we use the weight W in the following form:

$$W(\Delta t) = \frac{1}{(1 + \Delta t^2)^2} \quad (1)$$

3.2 Stereo Pléiades DEM

We use a stereo pair of Pléiades images acquired on 29th of May 2015, over an area of 309 km² to compute a high resolution 2-m digital elevation model (DEM). The stereo pairs are characterized by a baseline to height ratio (B/H) of 0.24 (e.g. Lacroix et al., 2013). Such low value of B/H makes the pair highly suitable for DEM generation, with minimal sampling problems on steep slopes (Lacroix et al., 2015). Previous studies using Pléiades pairs with B/H around 0.2-0.3 show DEM relative uncertainties on vegetation-free areas of 0.7–0.9 m (Berthier et al., 2014; Lacroix et al., 2015).

We use the open-source software Ames Stereo Pipeline developed by NASA (Shean et al., 2016), and the methodology developed in Lacroix (2016) to generate the DEM. We first orthorectify the images using a low resolution DEM (30 m), to remove the long-wavelength stereo component. Correlation of the resulting ortho-images allows a more efficient retrieval of the higher-frequency stereo component, which is then used to refine the low resolution DEM. This iterative process also helps to reduce artifacts on steep slopes (Lacroix, 2016).

3.3 GNSS data

A network of 26 markers was installed on the landslide (Figure 1) and measured 7 times in between November 2015 and May 2017 (see SI) using precise GNSS campaigns (RTK GNSS with baselines less than 2 km). Uncertainties are centimetric, except for two of the markers (points #1 and #21), which display higher error and were thus removed from our analysis. The average time separation between the GNSS campaigns and Landsat-8 acquisitions is ~8 days (20 days maximum).

215 **4 Results**

216 **4.1 Landsat-8 optical displacement time series: initial results**

217 The time series of the EW and NS components are shown in Figure 3 for a single
 218 location in the middle of the landslide body, representative of the landslide motion. We
 219 observe that the displacement is not linear with time (Figure 3a and 3b). The time-series
 220 is composed of three main signals: (1) a seasonal oscillation (Figure 3c), with metric am-
 221 plitudes, and a high degree of spatial variability across the area, (2) a sudden acceler-
 222 ation between March and July 2016 (Figures 3 and 4), and (3) an inter-annual non-linear
 223 trend that increases with time, particularly following the period of rapid acceleration (Fig-
 224 ures 3 and 4).

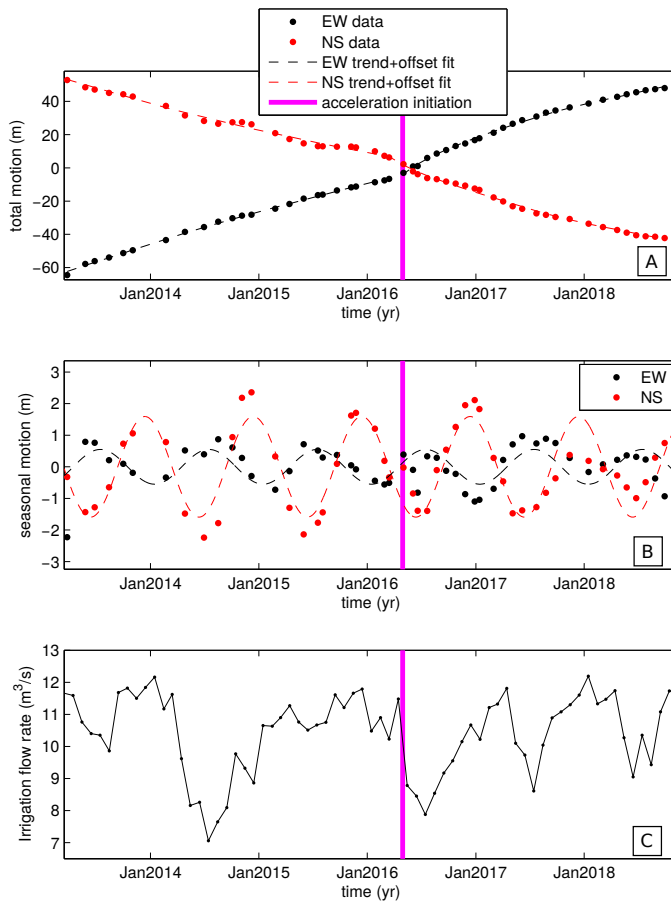


Figure 3. Horizontal motion for one selected point on the middle of the landslide over the 5.7 years of Landsat-8 images. A: Time-series of displacement anomaly (in m). The displacement anomaly is expressed relatively to a reference (zero displacement) taken in September 2015. Northward and Eastward are positive motions. Dashed lines represent the non-linear trend fitted to the data as well as the May 2016 offset. B: Time-series of displacement anomaly (in m) along EW and NS directions once the trend and the May 2016 offset are removed. The dashed curves represent the fitted sinusoid to the seasonal displacement. C: Mean monthly irrigation flow rates (in m^3/s) of the Pampa Majes canal.

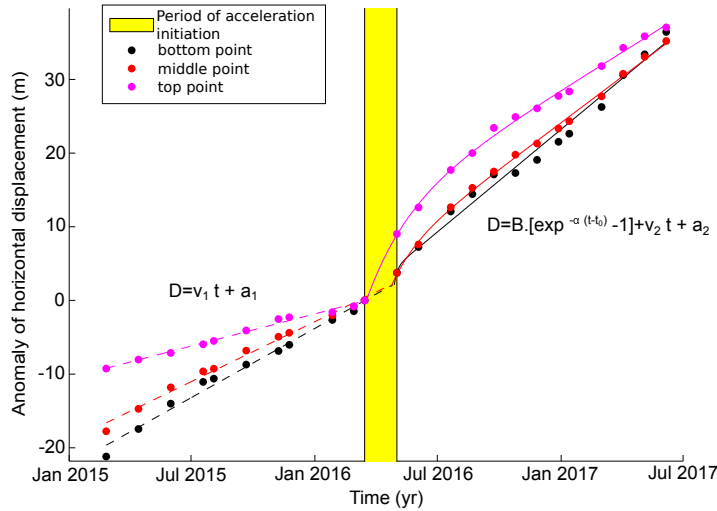


Figure 4. Displacement anomaly of horizontal motion relatively to a reference taken in March 2016, at three locations on the landslide (top, middle, lower part) for a period around May 2016. The plain lines show the best fit of the mathematical model combining the sudden acceleration and the linear trends before and after this sudden event (see text and equation 4 for details of the different parameters).

225 4.2 Landsat-8 optical displacement time series: data decomposition and 226 post-processing

227 To evaluate the amplitudes and the origins of the seasonal oscillations, the sudden
228 acceleration, and longer-term increase in landslide motion, we model the observed vari-
229 ations at each pixel (i,j) and for each component c (i.e. EW or NS) using several basis
230 functions. The seasonal component $S_{i,j,c}(t)$ is modelled using the following function:

$$S_{i,j,c}(t) = A_{i,j,c} * \cos(\omega t + \Phi_{i,j,c}) \quad (2)$$

231 where $\omega = \frac{2\pi}{365.25}$ is the oscillation frequency and A and Φ are the amplitude and day
232 of the year of the seasonal motion peak.

233 The sudden acceleration $Acc_{i,j,c}(t)$ is modelled using an exponential function of time:

$$Acc_{i,j,c}(t) = B_{i,j,c}[\exp^{-\alpha_{i,j,c}(t-t0_{i,j,c})} - 1] \quad if \ t > t_0 \quad (3)$$

234 where $\alpha_{i,j,c}$ is the characteristic time of the decay, and $t0_{i,j,c}$ is the time of the sudden
235 motion initiation.

236 Because of the non-linear inter-annual evolution of the landslide, it is challenging
237 to model the entire time-series with a simple mathematical function. Therefore, we es-
238 timate the different components successively:

- 239 1. To evaluate the characteristics of the sudden acceleration, we first approximate
240 the inter-annual motion as a linear trend for the year before March 2016 (of ve-
241 locity v_1) and for the year after July 2016 (of velocity v_2). The displacement val-
242 ues (D_c , where c denotes either the EW or the NS component) for each pixel (i,j)
243 can then be expressed by (Figure 4):

$$D_{i,j,c}(t) = v1_{i,j,c} \times t + a1_{i,j,c} \quad if \ 15/03/2015 < t < 15/03/2016 \quad (4)$$

$$D_{i,j,c}(t) = v2_{i,j,c} \times t + a2_{i,j,c} + Acc(t) \quad \text{if } 21/07/2017 > t > 21/07/2016 \quad (5)$$

where $a1_{i,j,c}$ and $a2_{i,j,c}$ are inverted parameters of the linear fit.

We then estimate the different parameters $B_{i,j,c}$, $\alpha_{i,j,c}$, $t0_{i,j,c}$, $v1_{i,j,c}$, $v2_{i,j,c}$, $a1_{i,j,c}$, $a2_{i,j,c}$ by minimizing the difference between the model and the observations. This minimization, using the L2 norm, is first made using a grid search before optimization using a gradient descent method. Constraints are given to the different parameters; in particular, we impose the α and $t0$ terms to be the same for both EW and NS components. We also impose the $t0$ initial guess to be between 2016/03/15 and 2016/05/02, as observed in the Landsat-8 time-series (Figure 4). Moreover, we impose the B_{EW} and B_{NS} terms to have the same ratio as the $v2_{EW}$ and $v2_{NS}$ ratio. We therefore assume that the orientation of the sudden acceleration is similar to that of the general motion. This assumption is verified with the GNSS measurements.

2. To extract the seasonal motion from the time-series, we first remove the modelled acceleration $Acc(t)$ from the initial time-series. We then estimate the non-linear inter-annual displacement by smoothing the observed time-series using a kernel of 13 months. We remove this smoothed time-series. Finally, we fit the seasonal component using a sinusoidal function spanning the entire observation period using equation 2, which reveals the amplitude and phase of the seasonal motion at each pixel.

This two step process is iterated twice to provide more robust results. The second iteration is made on the initial time-series with the first seasonal oscillation iteration removed.

Finally, we define the longer term acceleration for one year following 15th March 2016, and 1st July 2016 (before/after the sudden acceleration), expressed in percent of the initial value, by:

$$LT_A = \frac{v2_c - v1_c}{v1_c} * 100 \quad (6)$$

Similarly we define the longer term acceleration LT_A_2 over a year between the periods 2015/03/15-2016/03/15 and 2017/07/01-2018/07/01.

4.3 Landsat-8 optical displacement time series: seasonal oscillations

The amplitude of the seasonal oscillation can reach up to 5 m, and displays a large variability over the entire area covered by the correlation. The oscillations affect both the landslide and surrounding stable regions. Furthermore, on the landslide the seasonal oscillation is not oriented in the direction of the landslide motion. Finally, no clear seasonal oscillation is observed in the GNSS time-series on the landslide. These three observations suggest the oscillations are not related to landslide motion, but are in fact artifacts related to the Landsat-8 data. We can thus exclude the seasonal variations of the irrigation volume as the cause of the observed seasonal oscillation. Seasonal irrigation could influence the landslide kinematics, albeit with lower amplitudes than the seasonal signal observed here. Previous studies have noted similar artifacts in correlations made with very-high resolution satellite images, especially on steep slopes or near tree cover where there is dramatic variation in cast shadows (Delacourt et al., 2004; Lacroix et al., 2015). In medium-resolution satellite data, similar artifacts have also been reported by Hollingsworth et al. (2017), who suppressed the noise substantially by correlating images only acquired at the same point in the season, thereby minimizing differences in illumination properties. Bontemps et al. (2018) also report a substantial increase in noise when correlating images acquired at different seasons. Given that the Sigüas region is largely free of vegetation, we therefore suggest that the seasonal pattern observed here is due to an artifact originating from changing illumination conditions between scene ac-

quisitions. Because the casting of shadows is strongly controlled by the interaction of incidence light with a 3D object, we expect the shadow content within a satellite image to correlate strongly with topography. Consequently, shadows will contribute to frequency content of a satellite image, and in turn influence the correlator when used to retrieve ground displacements. To address the origin of this signal and correct it, we estimate the relation between the oscillation amplitudes and the topography. We plot the amplitude of the oscillation estimated in the EW and NS time-series as a function of the slope gradient and aspect calculated over a DEM at 2 m resolution (Figure 5). We show the amplitude averaged over all pixels for each slope gradient and aspect class. We clearly note that amplitudes are higher for larger slopes, and for slopes oriented southward, i.e. away from the sun. The NS amplitudes are also twice as large as the EW amplitudes.

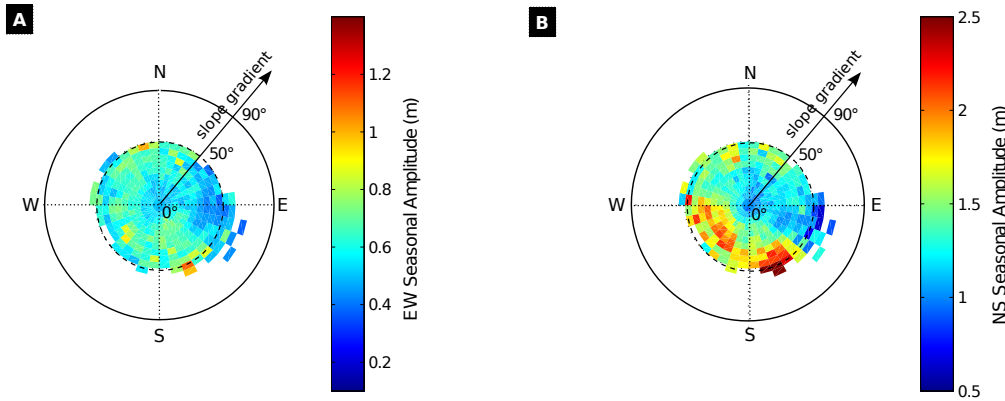


Figure 5. Amplitudes of the seasonal motion oscillations along EW (A) and NS (B) directions, represented as a function of the slope gradient (radial axis) and slope aspects (polar axis) of the topography calculated over the Pléiades DEM.

These observations emphasize the effect of changing shadows present within the Landsat-8 images. Indeed, Landsat-8 images are all acquired at 10:15 am local time, at which point the azimuth angle is oriented $\sim 030^\circ\text{N}$, which is exactly opposite to the slopes displaying the largest seasonal amplitudes (Figure 5). Furthermore, the elevation angles vary by about 20 degrees between summer and winter at these latitudes, causing the shadows from steep objects (see picture from Figure 2) to vary in size. Those variations are even larger when south-facing slope angles increase (in the southern hemisphere).

These observations account well for the seasonal variations in apparent displacement in the NS component, but less well for the EW component. In particular, the sun azimuth also varies between summer and winter, and should also cause the EW component to vary (albeit to a lesser extent). However, the topography is quite irregular, suggesting that non-linear effects may arise from the interaction between complex surface topography and sun illumination characteristics.

Finally, to isolate the real displacement signals relating to landslide kinematics, we remove the seasonal oscillations from our time-series by subtracting the best-fit sine wave over the whole time-series period.

4.4 Uncertainties of the Landsat-8 optical displacement time series

The Landsat-8 displacement time-series are compared to the GNSS measurements obtained on seven different dates. We compare both the raw time-series and the time-

series corrected from the seasonal oscillation. As seen in section 4.3, part of this seasonal oscillation is an artifact originating from the images used in the correlation. Because the dates of Landsat-8 and GNSS measurements can differ by up to 20 days (8 days in average), we interpolate the Landsat-8 displacement time-series on the GNSS campaign dates using linear interpolation. The comparison in both EW and NS directions is shown on Figure 6 and Table 1. The comparison shows a clear linear correlation, with a slope of the linear regression close to 1 (0.97 and 1.02) for both datasets, thus highlighting the potential of medium-resolution satellite data with high temporal sampling to retrieve landslide motion from space. The uncertainties evaluated by the RMSE between satellite and fields measurements yields values of 1.12 m (NS) and 1.55 m (EW), respectively; about one tenth of the input pixel resolution. This value is therefore better than previous estimates using medium resolution images over longer time-periods (Bontemps et al., 2018). It must be noted that the linear fit tends closer to 1, and the uncertainty is reduced by 50% when the seasonal correction is removed from the NS component (Table 1). This emphasizes the periodic bias introduced by the seasonal variation in illumination conditions.

Nevertheless, the error statistics for the EW component are not significantly improved by removing the seasonal signal. This could result from either (1) an artifact produced when the images are constructed (the orbit of Landsat-8 is aligned almost along the NS direction at our latitude of study area), (2) the non-linear influence of sun illumination on the EW component, and/or (3) difficulties in robustly quantifying the EW component of the seasonal illumination due to its lower amplitude compared with the NS component (see Figure 5).

The spatial variation of the uncertainty (RMSE) also shows larger errors close by the headscarp and at the bottom part of the landslide, close by a main secondary scarp (Figure 7). This highlights the effect of the correlation window size in areas of strong velocity heterogeneities (Bontemps et al., 2018).

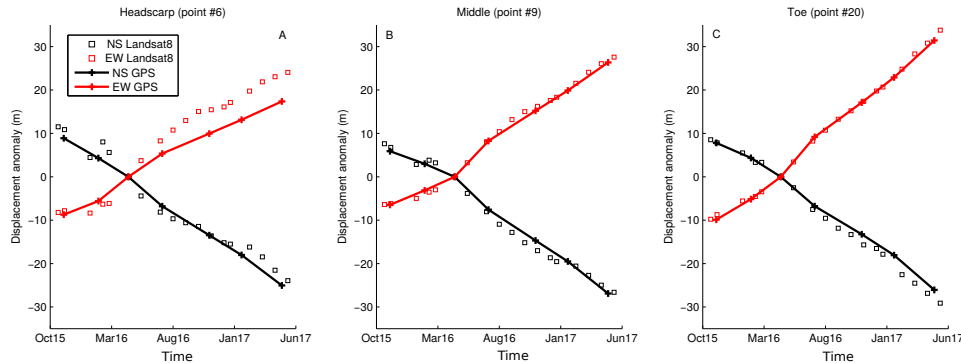


Figure 6. Time-series of displacement anomaly (in m) from GNSS and Landsat-8 satellites for both the NS and the EW component (Eastward and Southward are positive), for 3 selected points on the Siguas landslide: on the upper part (A), on the middle part (B), at the landslide toe (C). The satellite time-series are corrected from their seasonal oscillation.

4.5 Landslide motions

For each pixel of the image, we compute the mean annual velocity and mean displacement orientation over the whole time-series (Figure 8). The mean annual velocity over the landslide reaches up to 35 m/year. The mean orientation is 140°N except on

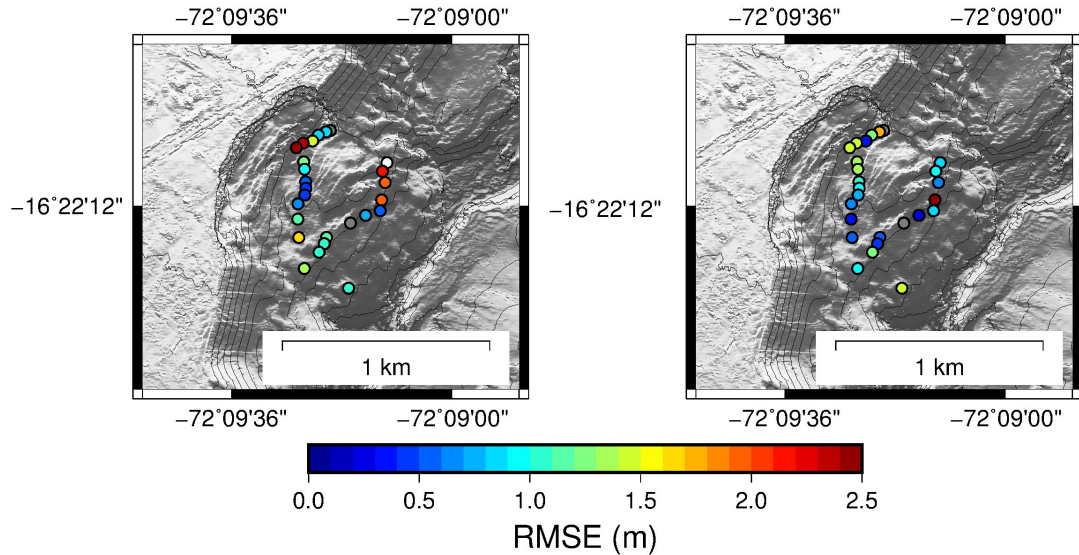


Figure 7. RMSE (in m) between GNSS and Landsat-8 measurements for both the EW (left) and the NS (right) components, calculated over the 7 dates of the GNSS campaigns.

Table 1. Statistics of errors between field and satellite measurements. β denotes the coefficient of the linear regression between field and satellite measurements.

processing level	RMSE EW (m)	RMSE NS (m)	β EW	β NS
raw time-series	1.55	2.24	1.02	0.90
seasonal oscillation corrected	1.55	1.12	1.02	0.97

the lower limits of the landslide, where orientations indicate a spreading of the material across the valley floor with a flow-like pattern of deformation at the landslide toe (Figure 8). The area affected by the landslide motion is about 0.9 km^2 . Its volume was previously estimated at $\sim 40 \text{ Mm}^3$ (Araujo, 2017) using a simple difference of two DEMs from 1996 and 2017. This volume is therefore certainly underestimated, because it does not take into account the center part of the landslide, where no ablation or accumulation occurs. The landslide consists of multiple rotational slides, with retrogressive motion of the head-scarp, and advancing motion of the body mass. The retrogressive motion is illustrated by the large acceleration at the headscarp after mid 2016 (section 4.6) and by the large change of morphology after a major displacement of the landslide crown (Figure 2). Using a visual analysis of Landsat8 images, 10 m resolution multispectral bands of Sentinel-2A satellite, and a field visit on 17th of April 2016, we can isolate the time-period for initiation of the headscarp retrogression between 31st March and 17th April 2016.

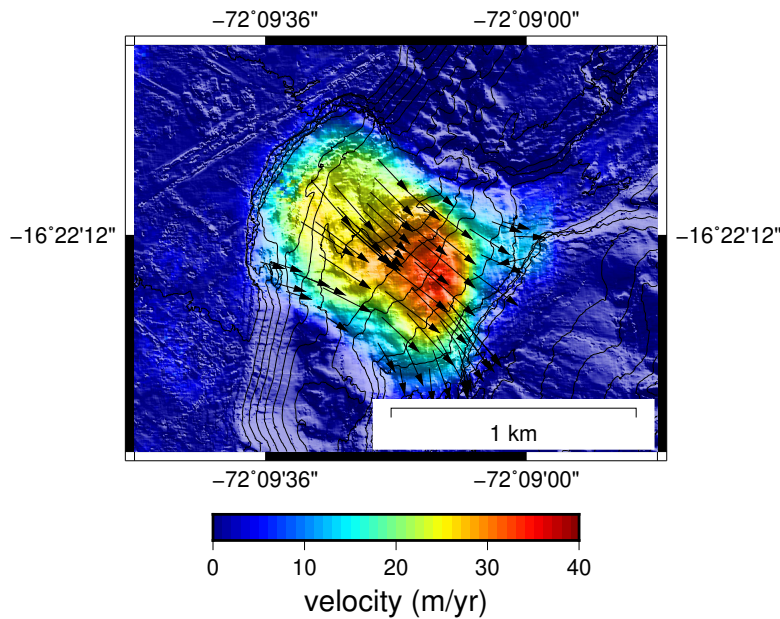


Figure 8. Mean annual velocity over the 5.7 years of Landsat-8 time-series (2013-2018). The vectors show the direction of the landslide flow. The circle refers to the point where time-series are shown in Figure 3.

4.6 April 2016 acceleration

Decomposing our time-series into several key signals (section 4.2) allows us to estimate two types of accelerations at two different time-scales (Figure 4): (1) a sudden acceleration in March-July 2016 (Equation 3, Figure 9), and (2) a longer acceleration after July 2016 (Equation 6). The following changes in velocity are also present in the GNSS time-series, albeit with a lower time resolution (Figure 10):

- The horizontal GNSS velocity shows an acceleration of the landslide over the whole period of observation.
- The horizontal GNSS velocity displays a period of higher velocities between February-July 2016. This transient motion appears to initiate earlier at the headscarp than downscarp. This transient motion is also clearly visible on the vertical component

of the GNSS, with an anomaly of all the points compared to the mean vertical velocity between February-July 2016. This anomaly (for all the points except five of them located on the lower part of the landslide) even shows an uplift of the landslide (positive vertical motion) in the period February-May 2016, followed by an important subsidence event in the period May-July 2016. The transient uplift is quantified by looking at the dip angle anomaly (angle of the motion vector in the vertical plane) during the February-May period (see Figures 10 and 11). The dip anomaly is clearly much larger close to the headscarp, reaching almost $+30^\circ$, before decreasing downscarp, with a $\sim 10^\circ$ anomaly in the middle of the slope. The lower part of the landslide displays more heterogeneous values, highlighting the complex structural character in this part of the slide.

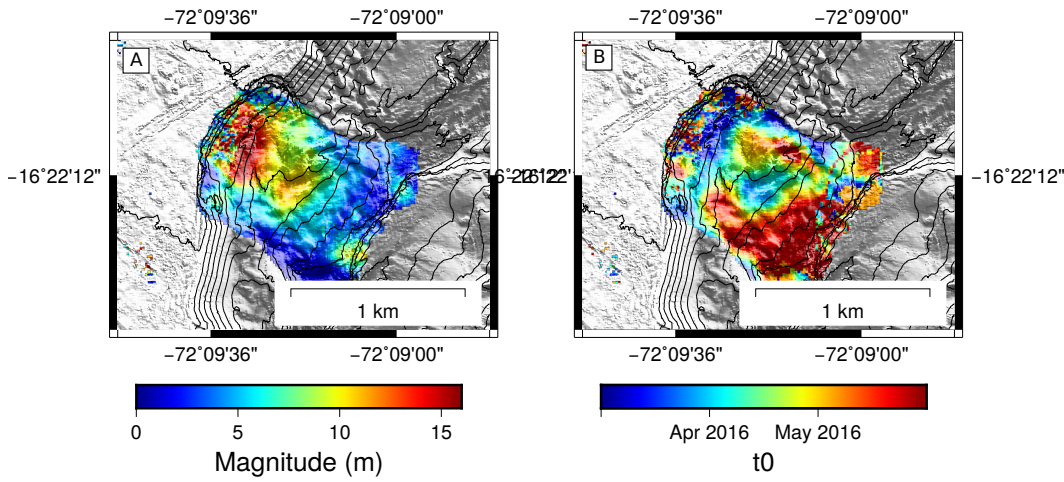


Figure 9. Characteristics of the transient motion of March-May 2016: (a) Magnitude (in m), (b) Initiation time. The grayed areas are pixels where the processing leads to no data.

The total horizontal magnitude ($\sqrt{B_{i,j,c=EW}^2 + B_{i,j,c=NS}^2}$) of the sudden acceleration Acc calculated from the satellite time-series reaches 15 m close to the headscarp, and decreases progressively downward in the landslide mass (Figure 9). The comparison of the velocity around this period estimated from Landsat-8 and GNSS is shown in Figure 10. The two datasets are consistent across the lower part of the landslide, displaying more variation towards the head of the landslide. For instance, at GNSS point #6, a clear discrepancy occurs in the horizontal velocity between January-June 2016 (Figure 10a). Furthermore, the onset of landslide acceleration at the headscarp is observed earlier on the Landsat-8 time-series than the GNSS time-series.

Our analysis also allows us to quantify the acceleration on an annual time-scale before and after the 2016 acceleration event. The parameter LT_A (equation 6) gives the change in velocity between the 2016-2017 period and the 2015-2016 period. It shows the headblock accelerating by more than 600% and a general and significant acceleration over the whole landslide mass (Figure 12a). 2016-2017 velocities increase by +135% just below the headscarp, and +50% below the main landslide mass compared to 2015-2016 velocities. This yearly acceleration is also observed in the GNSS time-series (Figure 10); however the GNSS analysis is somewhat limited due to the short coverage of the GNSS observations prior to March 2016, thus impacting the annual 2015-2016 velocity estimation. The 2017-2018 velocities indicate the motion is progressively slowing down, returning to its previous 2016 values by the end of 2018 (Figure 12b).

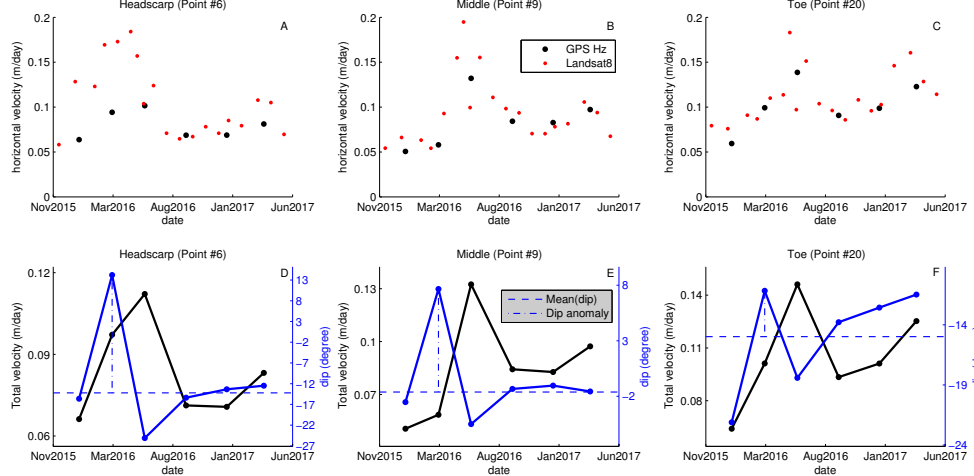


Figure 10. Time-series of horizontal motion (A-B-C) at 3 GNSS locations (Headscarp (Point 6), Middle (Point 9) and landslide toe (Point 20), located in Figure 11), aligned along an up-down profile in the landslide mass. In subplots (A,B,C) black dots corresponds to GNSS measurements, and red dots to the Landsat8 time-series. Subplots (D,E,F) represent the velocity vector measured by GNSS, decomposed as a magnitude (black curve) and a vertical angle (blue curve). The dash dotted blue line corresponds to the dip (vertical angle) anomaly observed in between February and May 2016, and represented in Figure 11.

5 Discussion

Our observations indicate multiple time-scales of landslide evolution. Initiation of the landslide has previously been suggested to result from water infiltration from irrigation (Hermanns et al., 2012). This conclusion is also consistent with the prevalent location of active landslides on the north-western flanks of the valley, where irrigation programs are in operation. The first signs of landslide activity were visible in 2004, 23 years after the beginning of irrigation in the area. We also notice the landslide initiates directly after the installation of the milk factory. This observation suggests that either (1) the observed motion is a direct effect of the milk factory installation and subsequent release of ground water, or (2) that water infiltration by irrigation has a long time delay before it begins to trigger landslides. In both cases, water infiltration coming from anthropogenic forcing must be a predominant cause of destabilization in highly weathered sediments found in dry deserts.

The mean pattern of velocity over the whole time-period suggests an advancing motion of the landslide mass, with velocities increasing toward the toe (Figure 8). This pattern is classically observed in landslides affecting incised river valleys (e.g. Lacroix et al., 2015), and can be explained either by thinner sediments occurring close by the landslide toe, and/or evacuation of sediments by river erosion.

The sudden acceleration of the landslide body observed in March-May 2016 does not coincide with any increase in rainfall or irrigation volume (Figure 3), thus precluding variation in water-flow as the trigger for acceleration. However, the sudden acceleration is well correlated with the timing of the headscarp retrogression estimated from a combination of Sentinel-2/Landsat8 images and a field survey between 31/03/2016 and 17/04/2016. GNSS data also show an upward motion immediately prior to the acceler-

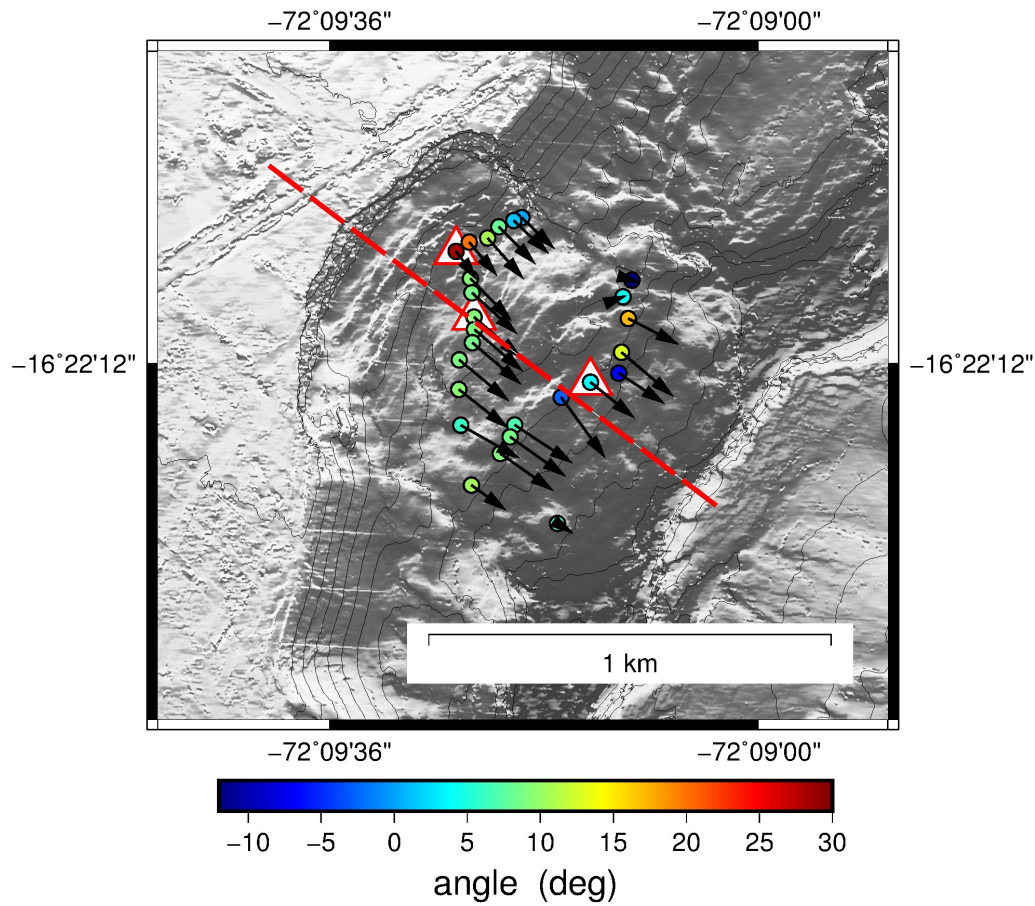


Figure 11. Anomaly of vertical angle (in degrees), calculated for all the GNSS time-series in between February and May 2016 (see text and Figure 10 for explanation). The red and white triangles shows the location of the GNSS markers whose time-series are represented in Figure 10. The red dashed line shows the location of the cross-section represented in Figure 13.

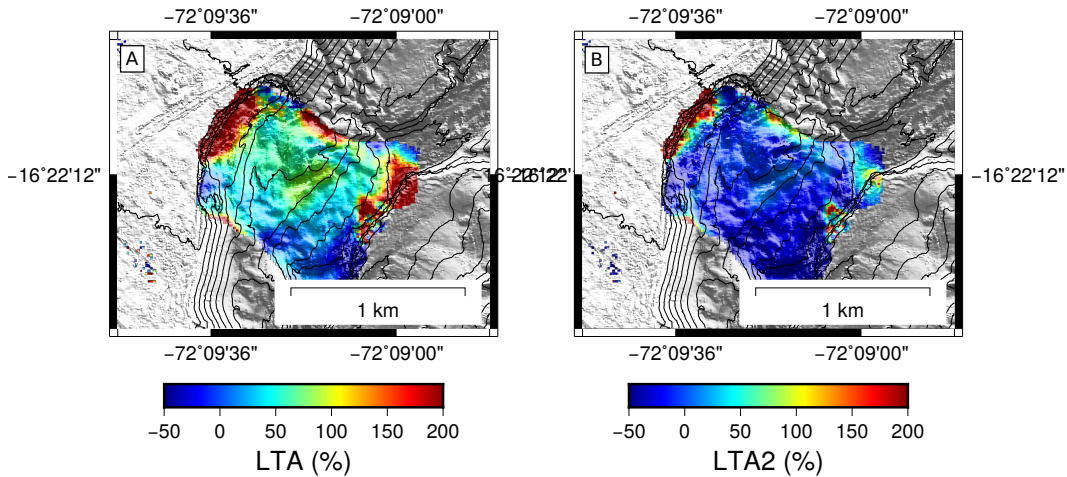


Figure 12. Velocity increment (expressed in percentage of the initial velocity value) between the period March 2015 - March 2016 and the period A: July 2016-June 2017 or B: July 2017-June 2018. The grayed areas are pixels where the processing leads to no data.

ation phase, which indicates that the mechanism of this acceleration is different from just a progressive motion. Furthermore, the landslide acceleration is larger (in percentage of the mean motion) upward than downward, which indicates the forcing is situated close to the landslide headscarp. Therefore, we conclude the landslide acceleration is caused by headscarp retrogression.

This sudden acceleration is also followed by higher velocities of the landslide, at least over annual scales (Figure 12). This highlights the effect of the headscarp retrogression and subsequent supply of sediment to the landslide mass. Previous studies also noticed an acceleration of landslide movements following a period of sediment supply, based on debris flows on the landslide body (Booth et al., 2018), or the triggering of debris flow after sediment supply (Budetta, 2010). In these different cases, the timing of the onset of acceleration is not clearly resolved, which makes the interpretation of the activation mechanism challenging. On the Sigüas landslide, the two different time-scales of acceleration suggest two physical processes are operating in the landslide; during, and following the headscarp collapse. The observed pattern of motion also shows that the destabilization is a self-entrainment process, where the motion of the advancing landslide mass destabilizes the headscarp, that then supplies sediment to the landslide body, resulting in acceleration. Our time-series also shows the landslide velocity progressively slows down, reaching in 2018 almost similar values than those before the sudden event. These observations highlight a relaxation process for the acceleration pulse that lasts at least 2 years. We can expect this retrogressive motion to stop after several iterations, since the newly generated blocks at the headscarp become less and less deep because of the flat terrain at the crown of the landslide. In steeper terrains, this self-entrainment process could be much longer to vanish.

The time-series of displacements documented here present a unique opportunity to study the interaction between the advancing and retrogressive motion of a landslide body and headscarp, respectively. Timing of the headscarp retrogression shows that the headscarp motion initiated in the first 17 days of April 2016, which is consistent with the date indicated in our Landsat-8 time-series, for the top of the landslide mass (see Figure 9). This date is actually not consistent with the GNSS observations in the same area. On the upper part of the landslide mass, close to the headscarp, the acceleration is observed on the Landsat-8 time-series before the GNSS data (Figure 10). Furthermore, the Landsat-8 time-series display larger motions than GNSS in the period February-June 2016 at the headscarp (Figure 6A). During this time period the landslide mass and its headscarps have very distinct motions (Figure 10). The size of the correlation windows used here (32 pixels, i.e. 480 m) encompass areas of heterogeneous velocity. Therefore, we suspect the difference between the Landsat-8 and GNSS time-series at the headscarp is due to the very different spatial scale over which the measurements were made, as already shown by previous studies (e.g. Bontemps et al., 2018). Strong image decorrelation also affects these measurements, further highlighting the large differential motions between the headscarp and its surroundings. This analysis suggests that the observed displacement time-series at the top of the landslide mass partly measures the velocity of the headblock. Furthermore, horizontal velocities at the top of the landslide body show a longer period of acceleration than downwscarp, in the center of the landslide body; lasting from January to June 2016 (Figure 10). Taken together, these observations all indicate that the headblock follows a gradual motion with time, and not a sudden collapse. This conclusion is also confirmed by the general oberved morphology, where coherent blocks are preserved during this motion (Figure 2).

Our observations are summarized in Figure 13, which shows a cross-section across the landslide body (Figure 13), where we infer the basal geometry of the landslide rupture using all available information, including topography, multi-temporal GNSS velocities and the Landsat-8 time-series. The velocity pattern is estimated separately during the advancing period (Figure 13a) and the retrogressive period (Figure 13b). Based on

Figure 13 and our observation of slow headblock motion with time, several mechanisms can be evoked to understand the subsequent landslide body acceleration: (1) overloading that provokes an increase in basal shear stress (Van Den Eeckhaut et al., 2013), (2) fluctuations of pore-water pressure due to rapid loading (Iverson & LaHusen, 1989), and (3) stress increase due to headblock pushing (Nishii & Matsuoka, 2012). To help to address these questions, we look at the vertical motions from GNSS data (Figures 10 and 11). GNSS velocities show a vertical anomaly during the retrogressive phase. This upward motion suggests that an increase in shear stress at the landslide base due to overloading, or fluctuations in pore-water pressure do not contribute to the acceleration of the landslide body. Therefore, this vertical signal suggests either a bulk compression of the material, thrusting of the upper blocks over the lower ones, or a global tilt of the compressed blocks due to the vertical push from the new headblocks. From the Landsat-8 dataset alone it is difficult to differentiate between a localized versus volumetric deformation, as the large correlation window size (32 pixels, i.e 480 m) smooths the displacement field over relatively large areas.

Thrusting of the upper blocks over lower ones could be possible, although thrust faults are not observed in the field. Moreover, such thrust faults would not explain the succession of upward and then an anomalous downward motions (see Figure 10). Tilting of the different blocks due to compression of the headblock is a plausible explanation classically used by dendrogeomorphologists (e.g. Clague, 2010), at least during the early phase of the headblock formation. Indeed, while the headblock failure surface is not sufficiently mature to start the tertiary creep phase, the headblock will push the lower block with a higher stress at the top of the lower block compared to the landslide base (see Figure 14). Therefore the headblock may act as a wedge (Figure 14), causing it to tilt downslope. Due to the separation of the landslide into several distinct blocks, this tilt may affect other downward blocks, in a domino fashion (Figure 14), thereby explaining the observed upward motion of all the other blocks (with decreasing magnitudes downslope).

This wedge effect may occur during all periods of headblock formation and failure surface maturation. As soon as the block is sufficiently decoupled from the landscape, the tertiary creep phase begins, with sliding occurring along the newly generated failure surface. Consequently, during this second phase the headblock no longer acts as a wedge, but as a basal constraint. Thus tilting will stop and the normal mechanism of sliding along the failure surface will start again. This explanation is consistent with GNSS observations that display vectors dipping back towards previous values (Figure 10). The anomalous downward motion immediately following the upward motion can thus be explained as a relaxation of the tilting once the sliding starts. This transient process of tilting is clearly observed in the GNSS data, with a short upward motion and no clear acceleration.

The general acceleration observed after tilting suggests a push from the collapsed headblock on the downward mass. We should note that this general acceleration in the year after the headblock collapse spatially decreases down the landslide. Velocity increases by +135% at the top of the sliding mass, compared to +50% on its lower part (Figure 12). Therefore, headblock pushing is efficient, at least over yearly time-scales. Our data suggests that the landslide velocity returns to the pre-retrogression phase values after only 2 years. When expressed in absolute values, the yearly acceleration is fairly constant over the whole landslide with around +13 m/year increase in velocity, except on the lowest block close to the river (+17 m/year). This highlights the strong coupling between the upper blocks. We suspect the lowest block behaves differently because of the higher slope gradient coupled with the complex structure, in addition to a very well defined head scarp on this block.

Accepted Article

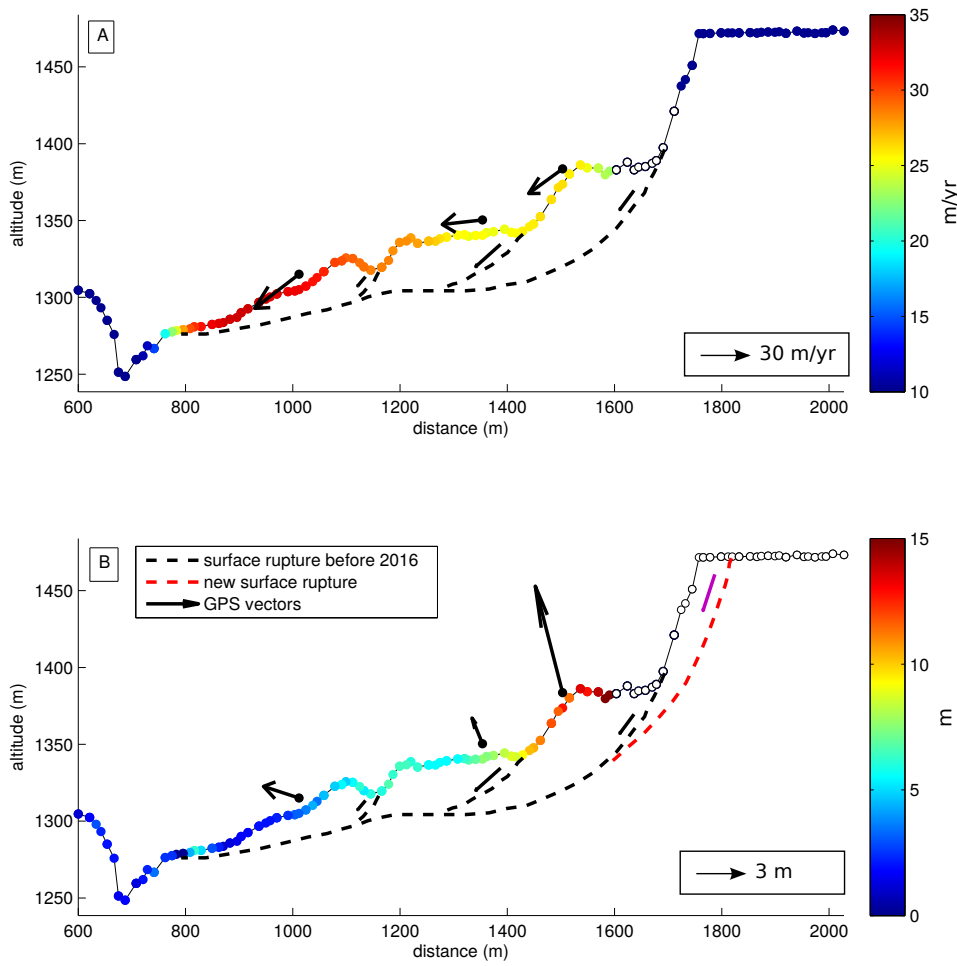


Figure 13. (A) Profile of the mean horizontal velocity (in m/yr) over the A-B segment noted in Figure 11. (B) Profile of the 2016 horizontal motion anomaly (in m) measured using equation 3. GNSS vectors are shown at 3 specific locations (with black arrows) in the distal plane for the two periods: on subplot (A) is represented the mean velocity vector, on (B) is represented the GNSS motion anomaly during the February 2016-May 2016 period, covering the period of the crown initial destabilization. The different slip surface are estimated from both the topography, the secondary scarps observed on the field and on the Pléiades DEM, and the GNSS velocity pattern. Vertical scales is exaggerated 3 times.

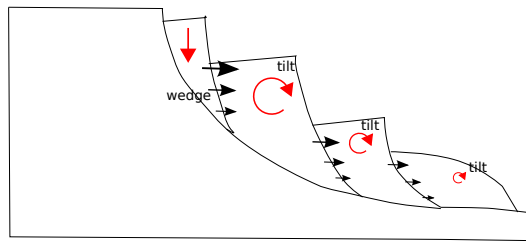


Figure 14. Schematic representation of the mechanics of the Siguas landslide during the initial phase of the headscarp retrogression.

536 6 Summary and Conclusions

37 We focus our analysis on a major landslide in an arid desert initiated by anthropogenic forcing, i.e. water infiltration, which results either from local irrigation, or installation of a nearby milk factory. Based on the analysis of more than 4 years of satellite images with frequent revisit times, we detect successive retrogressive and advancing phases of the landslide motion. Once initiated, the landslide kinematics follows a self-entrainment process where the headscarp retrogression supplies the main landslide body, that in turn accelerates and then destabilizes the headscarp. The combination of satellite images and GNSS campaigns allows us to investigate the kinematics and mechanics of this destabilization process; which involves (1) an advancing phase, where sliding along the failure surface occurs, followed by (2) a retrogressive phase, where the slow failure of the headblock provokes tilting of downward blocks and subsequent pushing of the entire landslide mass. Acceleration of the mass then occurs once its failure surface matures, and all the blocks become well-connected.

50 The detection and analysis of this transient motion was made possible thanks to
 51 the short revisit time of the Landsat-8 satellite, and the analysis of the derived time-series
 52 of ground displacement. This processing involved a new approach to correcting artifacts
 53 arising from illumination changes in the satellite images, thereby reducing uncertainties
 54 (RMSE) on the ground motion on the landslide, $\sim 1/10$ th of a pixel size in both horizontal directions.
 55 The validation of this method for medium resolution (10-15 m) freely available global satellite data is a new step toward their regular use for studying small
 56 ($\sim 0.1 \text{ km}^2$) and slow ($\sim 1 \text{ m/yr}$) objects, such as landslides, rock- or ice- glaciers, and
 57 specifically for analyzing transient displacement signals. While the interest and development
 58 of community tools for processing InSAR time-series has exploded in recent years
 59 (e.g. Agram et al., 2013), few tools exist and are in place for deriving optical time-series.
 60 The combination of Landsat-7/8 and Sentinel-2 data, with 8 and 5 day revisit times re-
 61 spectively, can provide one image every 3 days at the equator, despite misregistration
 62 errors between orthoimages introduced during post-processing of the raw data (Storey
 63 et al., 2016). The generation of such detailed time-series over large regions will provide
 64 important constraints for studying the mechanics of gravitational motions in general, and
 65 understanding the deformation processes (both localized and bulk) that govern their de-
 66 velopment.

68 7 Acknowledgments

569 This research was financially supported by ESA through the Alcantara initiative
 570 Monitoring and Detection of Landslides from optical Images time-series (ESA 15/P26).
 571 This work is part of the joint program IRD-INGEMMET. The Pléiades images have been
 572 provided by Astrium and the ISIS/CNES program, and can be accessed through the As-
 573 trium repository <https://www.intelligence-airbusds.com/geostore/>. Landsat-8 images cour-

tesy of the U.S. Geological Survey, and can be accessed through the EarthExplorer repository <https://earthexplorer.usgs.gov/>. The GPS data are provided in the supplementary materials. The irrigation flow rates are provided by the autodema repository <https://autodema.gob.pe/>.

References

- Agram, P., Jolivet, R., Riel, B., Lin, Y., Simons, M., Hetland, E., ... Lasserre, C. (2013). New radar interferometric time series analysis toolbox released. *Eos, Transactions American Geophysical Union*, 94(7), 69–70.
- Altena, B., Scambos, T., Fahnestock, M., & Kääb, A. (2018). Extracting recent short-term glacier velocity evolution over southern alaska from a large collection of landsat data. *The Cryosphere Discussions*, 2018, 1–27. Retrieved from <https://www.the-cryosphere-discuss.net/tc-2018-66/> doi: 10.5194/tc-2018-66
- Amitrano, D. (2004). Emerging complexity in a simple model of the mechanical behaviour of rocks. *CR Geosciences*, 336(6), 505 – 512. Retrieved 2013-02-14, from <http://arxiv.org/abs/0709.3028> (Comptes Rendus Geosciences 336, 6 (2004) 505-512) doi: 10.1016/j.crte.2003.11.023
- Araujo, E. (2017). *Evolucion, dinamica, implicancias y monitoreo del deslizamiento de siguas, arequipa* (Unpublished doctoral dissertation). Universidad Nacional San Antonio Abad del Cusco.
- Bennett, G. L., Roering, J. J., Mackey, B. H., Handwerger, A. L., Schmidt, D. A., & Guillod, B. P. (2016). Historic drought puts the brakes on earthflows in northern california. *Geophysical Research Letters*, 43(11), 5725–5731.
- Berthier, E., Vincent, C., Magnússon, E., Gunnlaugsson, A., Pitte, P., Le Meur, E., ... Wagnon, P. (2014). Glacier topography and elevation changes derived from pliades sub-meter stereo images. *The Cryosphere*, 8(6), 2275–2291. Retrieved from <https://www.the-cryosphere.net/8/2275/2014/> doi: 10.5194/tc-8-2275-2014
- Bontemps, N., Lacroix, P., & Doin, M. (2018). Inversion of deformation fields time-series from optical images, and application to the long term kinematics of slow-moving landslides in peru. *Remote Sensing Environment*, 210, 144–158.
- Booth, A. M., McCarley, J., Hinkle, J., Shaw, S., Ampuero, J.-P., & Lamb, M. P. (2018). Transient reactivation of a deep-seated landslide by undrained loading captured with repeat airborne and terrestrial lidar. *Geophysical Research Letters*, 45(10), 4841–4850.
- Budetta, P. (2010). Rockfall-induced impact force causing a debris flow on a volcanoclastic soil slope: a case study in southern italy. *Natural Hazards and Earth System Sciences*, 10(9), 1995–2006. Retrieved from <https://www.nat-hazards-earth-syst-sci.net/10/1995/2010/> doi: 10.5194/nhess-10-1995-2010
- Calabro, M., Schmidt, D., & Roering, J. (2010). An examination of seasonal deformation at the portuguese bend landslide, southern california, using radar interferometry. *J. Geophys. Res.*, 115(F2).
- Carey, J., & Petley, D. (2014). Progressive shear-surface development in cohesive materials; implications for landslide behaviour. *Engineering Geology*, 177, 54–65.
- Clague, J. J. (2010). Dating landslides with trees. In *Tree rings and natural hazards* (pp. 81–89). Springer.
- Cruden, D., & Varnes, D. L. (1996). Landslide types and processes. In *Landslides: investigation and mitigation* (pp. 36–75). National Academy Press.
- Dehecq, A., Gourmelen, N., & Trouve, E. (2015, June). Deriving large-scale glacier velocities from a complete satellite archive: Application to the PamirKarakoramHimalaya. *Remote Sensing of Environment*, 162, 55–66. Retrieved 2016-10-03, from <http://linkinghub.elsevier.com/retrieve/pii/>

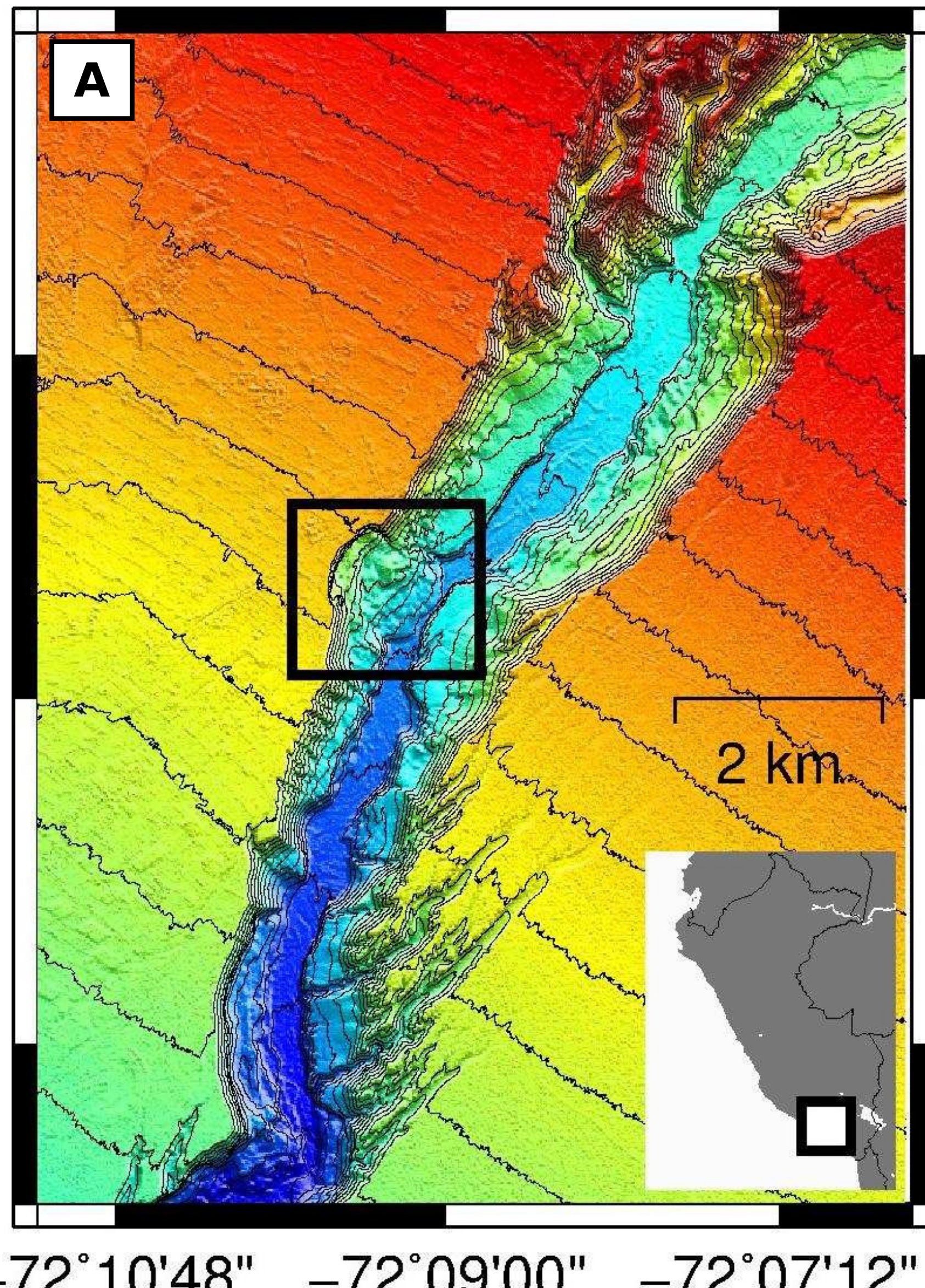
- 627 S0034425715000553 doi: 10.1016/j.rse.2015.01.031
 628 Delacourt, C., Allemand, P., Casson, B., & Vadon, H. (2004). Velocity field of the
 629 La Clapire landslide measured by the correlation of aerial and QuickBird satellite
 630 images. *Geophysical Research Letters*, 31(15), n/a–n/a. Retrieved 2014-
 631 02-24, from <http://onlinelibrary.wiley.com/doi/10.1029/2004GL020193/abstract> doi: 10.1029/2004GL020193
 632
- 633 Eberhardt, E., Stead, D., & Coggan, J. (2004, January). Numerical analysis of initiation
 634 and progressive failure in natural rock slopes - the 1991 Randa rockslide.
 635 *International Journal of Rock Mechanics and Mining Sciences*, 41(1), 69–87.
 636 Retrieved from <http://www.sciencedirect.com/science/article/pii/S1365160903000765> doi: 10.1016/S1365-1609(03)00076-5
 637
- 638 Fahnstock, M., Scambos, T., Moon, T., Gardner, A., Haran, T., & Klinger,
 639 M. (2015, November). Rapid large-area mapping of ice flow using Landsat 8.
 640 *Remote Sensing of Environment*. Retrieved 2016-10-03, from
 641 <http://linkinghub.elsevier.com/retrieve/pii/S003442571530211X>
 642 doi: 10.1016/j.rse.2015.11.023
 643
- 644 Federico, A., Popescu, M., Elia, G., Fidelibus, C., Interni, G., & Murianni, A. (2012,
 645 May). Prediction of time to slope failure: a general framework. *Environmental
 646 Earth Sciences*, 66(1), 245–256. Retrieved 2016-10-03, from <http://link.springer.com/10.1007/s12665-011-1231-5> doi: 10.1007/s12665-011-1231-5
 647
- 648 Gischig, V., Preisig, G., & Eberhardt, E. (2016). Numerical investigation of seismically
 649 induced rock mass fatigue as a mechanism contributing to the progressive
 650 failure of deep-seated landslides. *Rock Mechanics and Rock Engineering*, 49(6),
 651 2457–2478.
- 652 Handwerger, A. L., Roering, J. J., & Schmidt, D. A. (2013). Controls on the seasonal
 653 deformation of slow-moving landslides. *Earth and Planetary Science Letters*, 377, 239–247.
- 654 Handwerger, A. L., Roering, J. J., Schmidt, D. A., & Rempel, A. W. (2015). Kinematics
 655 of earthflows in the northern California coast ranges using satellite
 656 interferometry. *Geomorphology*, 246, 321–333.
- 657 Hendron, A., & Patton, F. (1985). *The vaiont slide, a geotechnical analysis based on
 658 how geologic observations of the failure surface* (Tech. Rep. No. 85 (5)). U.S.
 659 Army Corps of Engineers.
- 660 Hermanns, R. L., Valderrama, P., Fauqué, L., Penna, I. M., Sepúlveda, S., Moreiras,
 661 S., & Zavala Carrión, B. (2012). Landslides in the Andes and the need to communicate
 662 on an interandean level on landslide mapping and research. *Rev Asoc
 663 Geol Argent*, 69(3), 321–327.
- 664 Hilley, G., Brägmann, R., Ferretti, A., Novali, F., & Rocca, F. (2004). Dynamics of
 665 slow-moving landslides from permanent scatterer analysis. *Science*, 304(5679),
 666 1952–1955.
- 667 Hollingsworth, J., Ye, L., & Avouac, J.-P. (2017). Dynamically triggered slip on a
 668 splay fault in the mw 7.8, 2016 Kaikoura (New Zealand) earthquake. *Geophysical
 669 Research Letters*, 44(8), 3517–3525.
- 670 Hsu, Y.-J., Chen, R.-F., Lin, C.-W., Chen, H.-Y., & Yu, S.-B. (2014). Seasonal,
 671 long-term, and short-term deformation in the central range of Taiwan induced
 672 by landslides. *Geology*, 42(11), 991–994.
- 673 Iverson, R. M. (2000). Landslide triggering by rain infiltration. *Water Resources
 674 Research*, 36(7), 1897. Retrieved 2013-02-01, from <http://resourcelists.st-andrews.ac.uk/items/2D9E0D4D-5883-6C3F-349D-329E36BC06AD.html>
 675 doi: 10.1029/2000WR900090
- 676 Iverson, R. M., & LaHusen, R. G. (1989). Dynamic pore-pressure fluctuations in
 677 rapidly shearing granular materials. *Science*, 246(4931), 796–799.
- 678 Iverson, R. M., & Major, J. J. (1987, January). Rainfall, ground-water flow,
 679 and seasonal movement at Minor Creek landslide, northwestern Cali-

- 682 fornia: Physical interpretation of empirical relations. *Geological Society of America Bulletin*, 99(4), 579–594. Retrieved 2013-01-29, from
 683 <http://gsabulletin.gsapubs.org/content/99/4/579> doi: 10.1130/0016-7606(1987)99<579:RGFASM>2.0.CO;2
- 684 Kaab, A., Winsvold, S. H., Altena, B., Nuth, C., Nagler, T., & Wuite, J. (2016).
 685 Glacier remote sensing using sentinel-2. part i: Radiometric and geometric performance, and application to ice velocity. *Remote Sensing*, 8(7). Retrieved 686 from <http://www.mdpi.com/2072-4292/8/7/598> doi: 10.3390/rs8070598
- 687 Lacroix, P. (2016). Landslides triggered by the gorkha earthquake in the langtang valley, volumes and initiation processes. *Earth, Planets and Space*, 68(1), 46.
- 688 Lacroix, P., & Amitrano, D. (2013, December). Long-term dynamics of rockslides and damage propagation inferred from mechanical modeling. *Journal of Geophysical Research: Earth Surface*, 118(4), 2292–2307. Retrieved 689 2014-09-15, from <http://onlinelibrary.wiley.com/doi/10.1002/2013JF002766/abstract> doi: 10.1002/2013JF002766
- 690 Lacroix, P., Berthier, E., & Taipe, E. (2015, August). Earthquake-driven acceleration of slow-moving landslides in the Colca valley, Peru, detected from Pliades images. *Remote Sensing of Environment*, 165, 148–158. Retrieved 691 2016-10-03, from <http://linkinghub.elsevier.com/retrieve/pii/S0034425715300080> doi: 10.1016/j.rse.2015.05.010
- 692 Lacroix, P., Bièvre, G., Pathier, E., Kniess, U., & Jongmans, D. (2018, September). Use of sentinel-2 images for the detection of precursory motions before 693 landslide failures. *Remote Sensing of Environment*, 215, 507–516.
- 694 Lacroix, P., Perfettini, H., Taipe, E., & Guillier, B. (2014, September). Co- and 695 Postseismic motion of a landslide; observations, modelling and analogy with tectonic faults. *Geophysical Research Letters*, n/a–n/a. Retrieved 696 2014-09-15, from <http://onlinelibrary.wiley.com.biblioplanets.gate.inist.fr/enhanced/doi/10.1002/2014GL061170/#publication-history> doi: 10.1002/2014GL061170
- 697 Lacroix, P., Zavala, B., Berthier, E., & Audin, L. (2013, May). Supervised 698 Method of Landslide Inventory Using Panchromatic SPOT5 Images and Application to the Earthquake-Triggered Landslides of Pisco (Peru, 2007, Mw8.0). *Remote Sensing*, 5(6), 2590–2616. Retrieved 699 2014-04-22, from <http://www.mdpi.com/2072-4292/5/6/2590> doi: 10.3390/rs5062590
- 700 Leprince, S., Barbot, S., Ayoub, F., & Avouac, J.-P. (2007, June). Automatic 701 and Precise Orthorectification, Coregistration, and Subpixel Correlation of 702 Satellite Images, Application to Ground Deformation Measurements. *IEEE Transactions on Geoscience and Remote Sensing*, 45(6), 1529–1558. doi: 703 10.1109/TGRS.2006.888937
- 704 Leprince, S., Muse, P., & Avouac, J. P. (2008, Sept.). In-flight ccd distortion 705 calibration for pushbroom satellites based on subpixel correlation. *IEEE Transactions on Geoscience and Remote Sensing*, 46(9), 2675–2683. doi: 10.1109/TGRS.2008.918649
- 706 Locat, A., Leroueil, S., Bernander, S., Demers, D., Jostad, H. P., & Ouehb, L. 707 (2011). Progressive failures in eastern canadian and scandinavian sensitive clays. *Canadian Geotechnical Journal*, 48(11), 1696–1712.
- 708 Mountjoy, J. J., McKean, J., Barnes, P. M., & Pettinga, J. R. (2009). Terrestrial-style 709 slow-moving earthflow kinematics in a submarine landslide complex. *Marine geology*, 267(3-4), 114–127.
- 710 Nishii, R., & Matsuoka, N. (2012). Kinematics of an alpine retrogressive rockslide 711 in the japanese alps. *Earth Surface Processes and Landforms*, 37(15), 1641–1650.
- 712 Palmer, J. (2017). Creeping earth could hold secret to deadly landslides. *Nature*, 713 548(7668), .
- 714 Reid, M. E. (1994). A pore-pressure diffusion model for estimating landslide-

- 737 inducing rainfall. *The Journal of Geology*, 102(6), 709–717.
- 738 Schulz, W. H., Kean, J. W., & Wang, G. (2009, December). Landslide movement in
739 southwest Colorado triggered by atmospheric tides. *Nature Geoscience*, 2(12),
740 863–866. Retrieved 2014-10-13, from <http://www.nature.com/ngeo/journal/v2/n12/abs/ngeo659.html> doi: 10.1038/ngeo659
- 741 Shean, D. E., Alexandrov, O., Moratto, Z. M., Smith, B. E., Joughin, I. R., Porter,
742 C., & Morin, P. (2016). An automated, open-source pipeline for mass produc-
743 tion of digital elevation models (dems) from very-high-resolution commercial
744 stereo satellite imagery. *ISPRS Journal of Photogrammetry and Remote Sens-
745 ing*, 116, 101–117.
- 746 Storey, J., Roy, D. P., Masek, J., Gascon, F., Dwyer, J., & Choate, M. (2016). A
747 note on the temporary misregistration of landsat-8 operational land imager
748 (oli) and sentinel-2 multi spectral instrument (msi) imagery. *Remote Sensing
749 of Environment*, 186, 121–122.
- 750 Strozzi, T., Delaloye, R., Kaab, A., Ambrosi, C., Perruchoud, E., & Wegmüller, U.
751 (2010, March). Combined observations of rock mass movements using satel-
752 lite SAR interferometry, differential GPS, airborne digital photogrammetry,
753 and airborne photography interpretation. *Journal of Geophysical Research*,
754 115, 11 PP. Retrieved from <http://www.agu.org/pubs/crossref/2010/2009JF001311.shtml> doi: 201010.1029/2009JF001311
- 755 Stumpf, A., Malet, J. P., Allemand, P., & Ulrich, P. (2014, September). Surface
756 reconstruction and landslide displacement measurements with Pliades satellite
757 images. *ISPRS Journal of Photogrammetry and Remote Sensing*, 95, 1–12. Re-
758 trieval 2014-07-11, from <http://www.sciencedirect.com/science/article/pii/S0924271614001269> doi: 10.1016/j.isprsjprs.2014.05.008
- 759 Urgeles, R., & Camerlenghi, A. (2013). Submarine landslides of the mediterranean
760 sea: Trigger mechanisms, dynamics, and frequency-magnitude distribution.
761 *Journal of Geophysical Research: Earth Surface*, 118(4), 2600–2618.
- 762 Van Den Eeckhaut, M., Poesen, J., & Hervas, J. (2013). *Mass-movement causes:
763 overloading*. Academic Press.
- 764 Zerathe, S., Lacroix, P., Jongmans, D., Marino, J., Taipe, E., Wathelet, M., ...
765 Tatard, L. (2016, September). Morphology, structure and kinematics of a
766 rainfall controlled slow-moving Andean landslide, Peru: The Maca slow-moving
767 Andean landslide. *Earth Surface Processes and Landforms*, 41(11), 1477–1493.
768 Retrieved 2016-10-03, from <http://doi.wiley.com/10.1002/esp.3913> doi:
769 10.1002/esp.3913

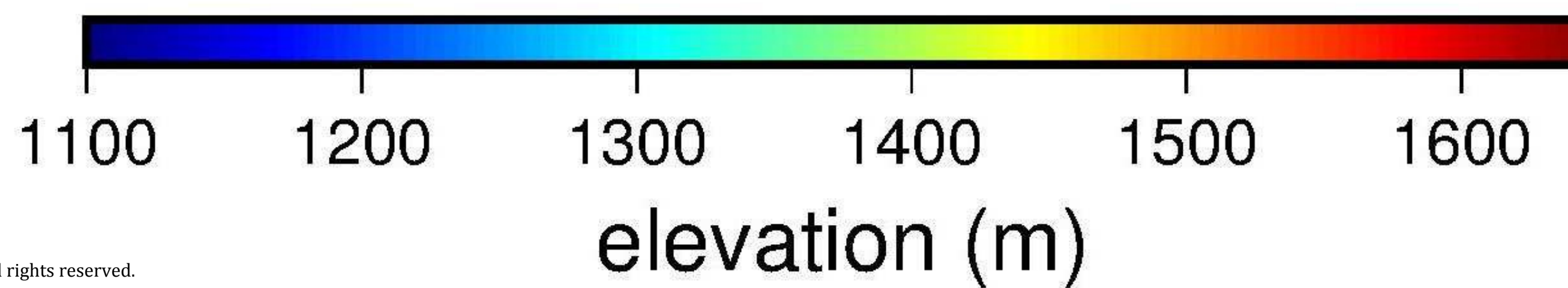
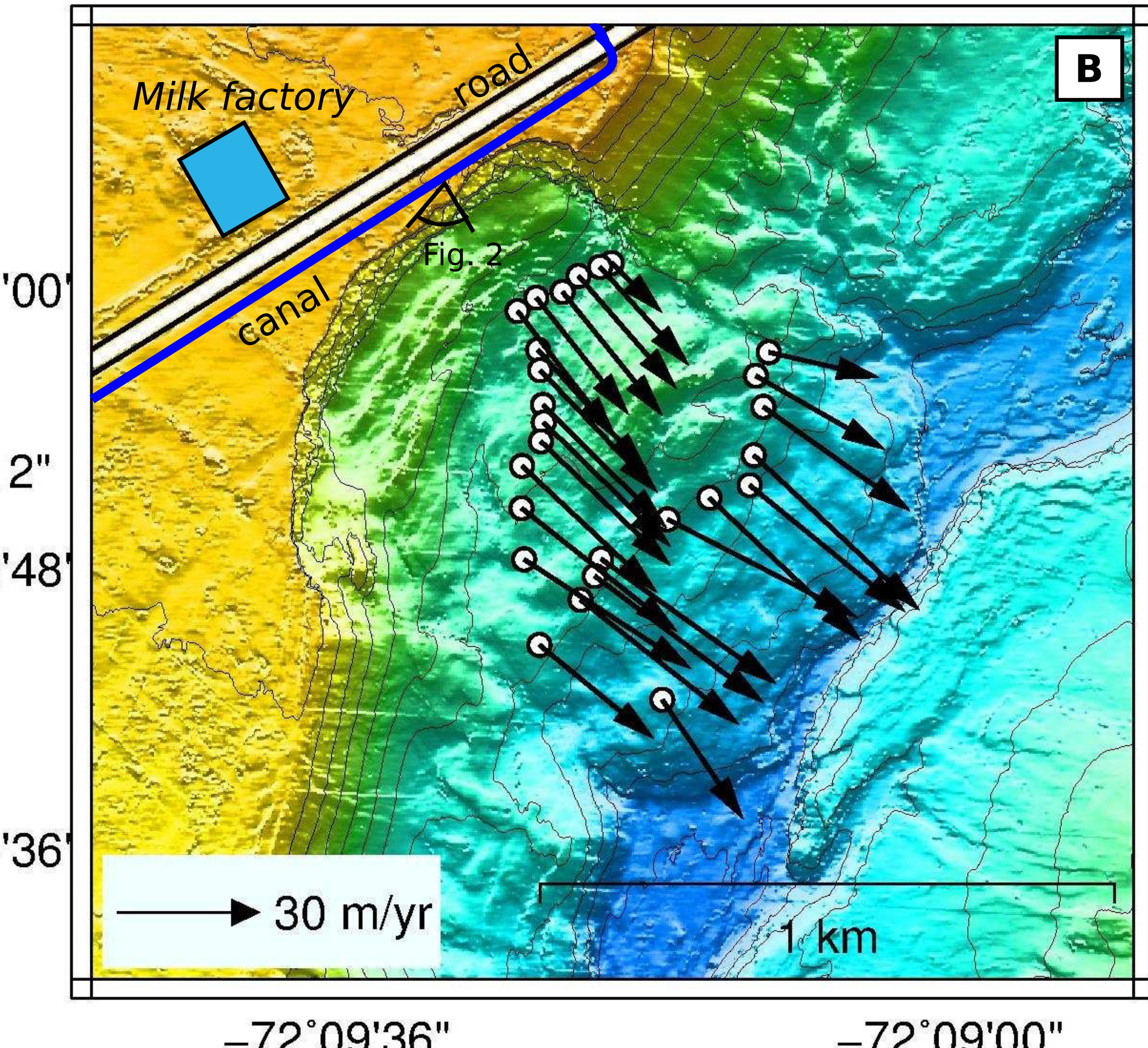
Accepted Article

-72°10'48" -72°09'00" -72°07'12"



-72°09'36"

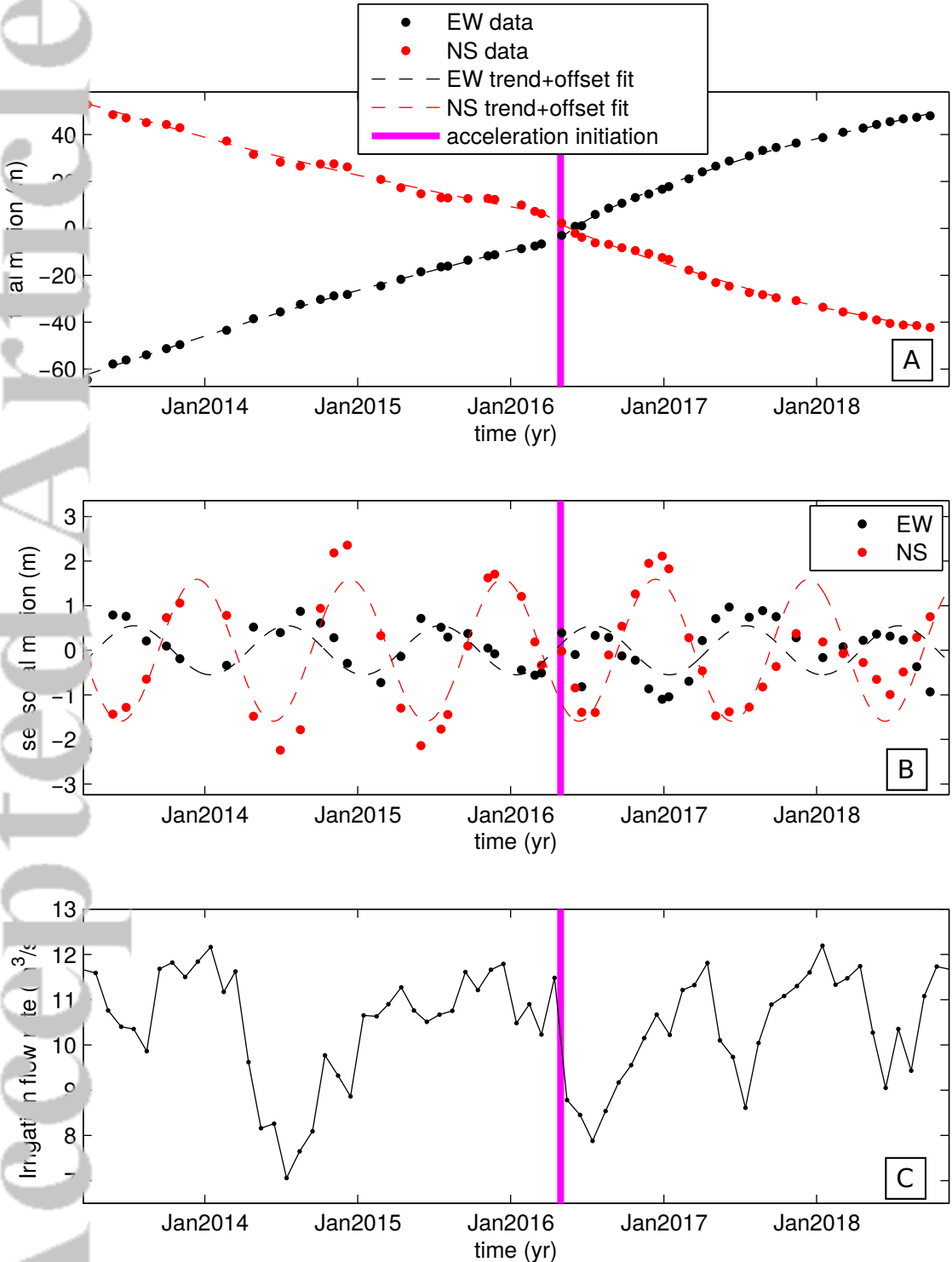
-72°09'00"



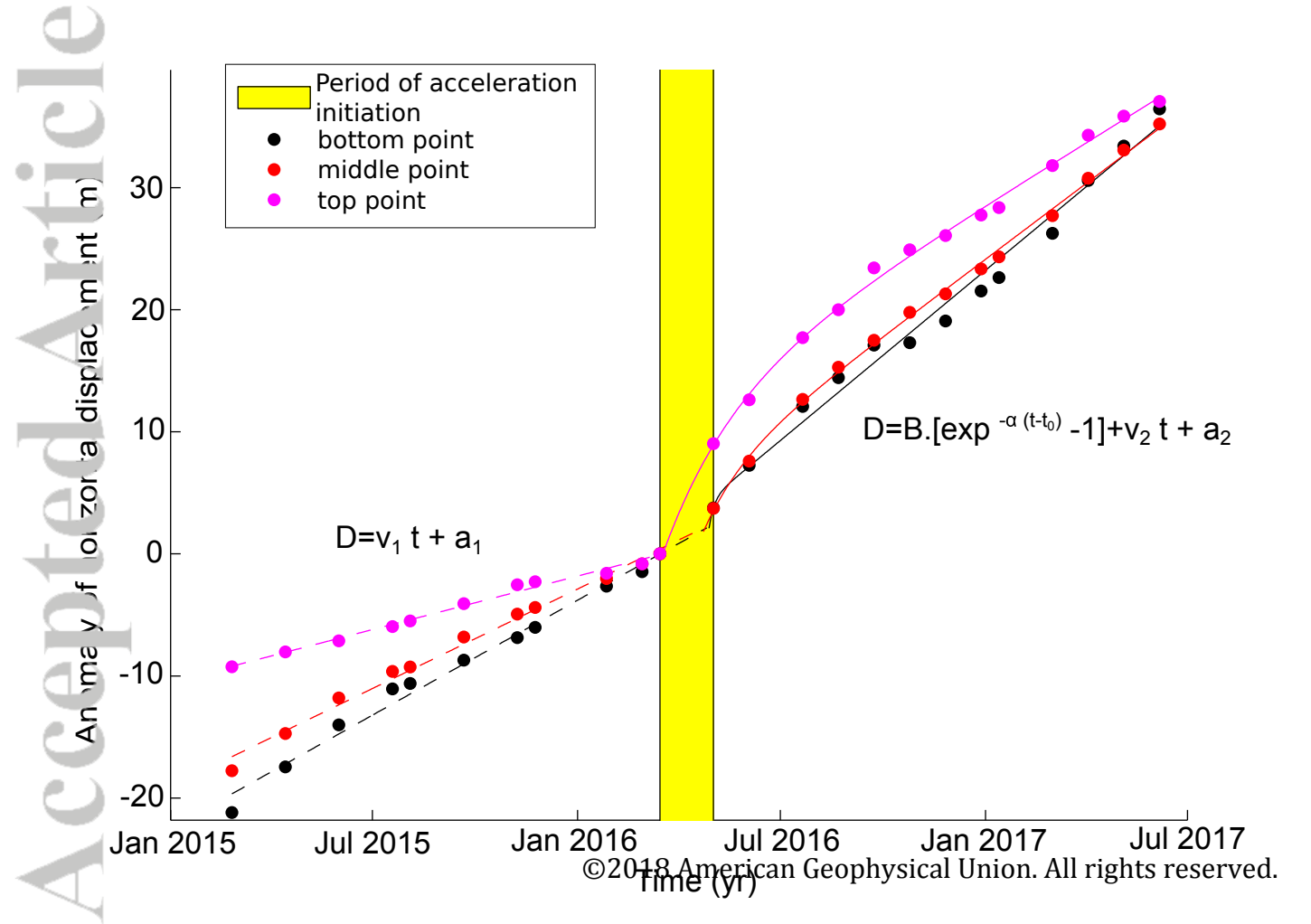
Accepted Article



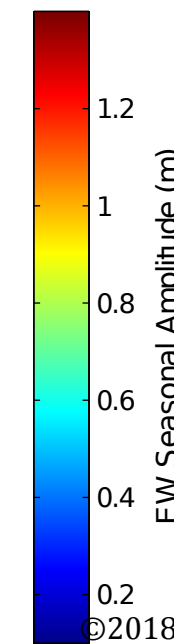
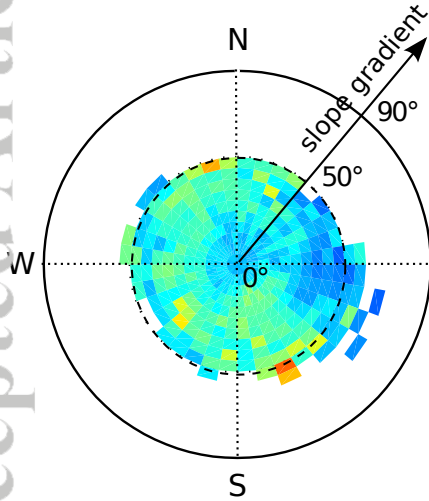
Accepted Article



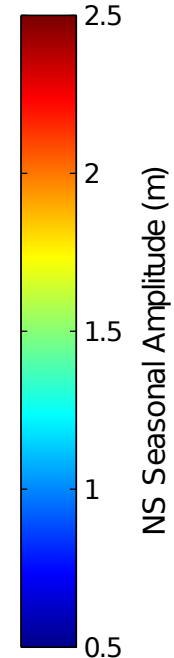
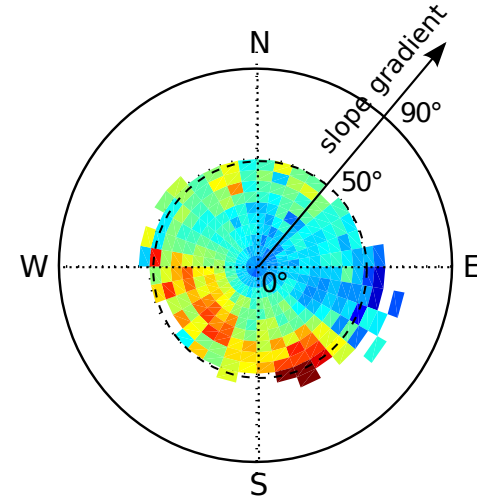
Accepted Article



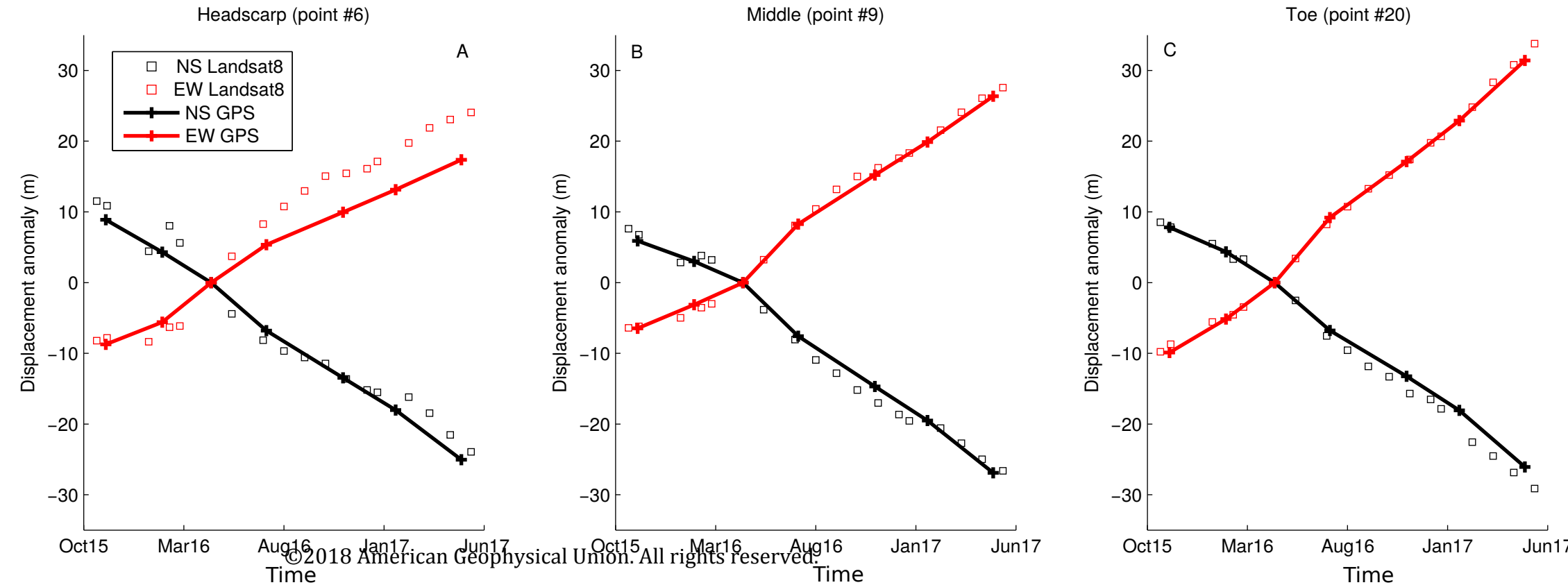
Accepted Article



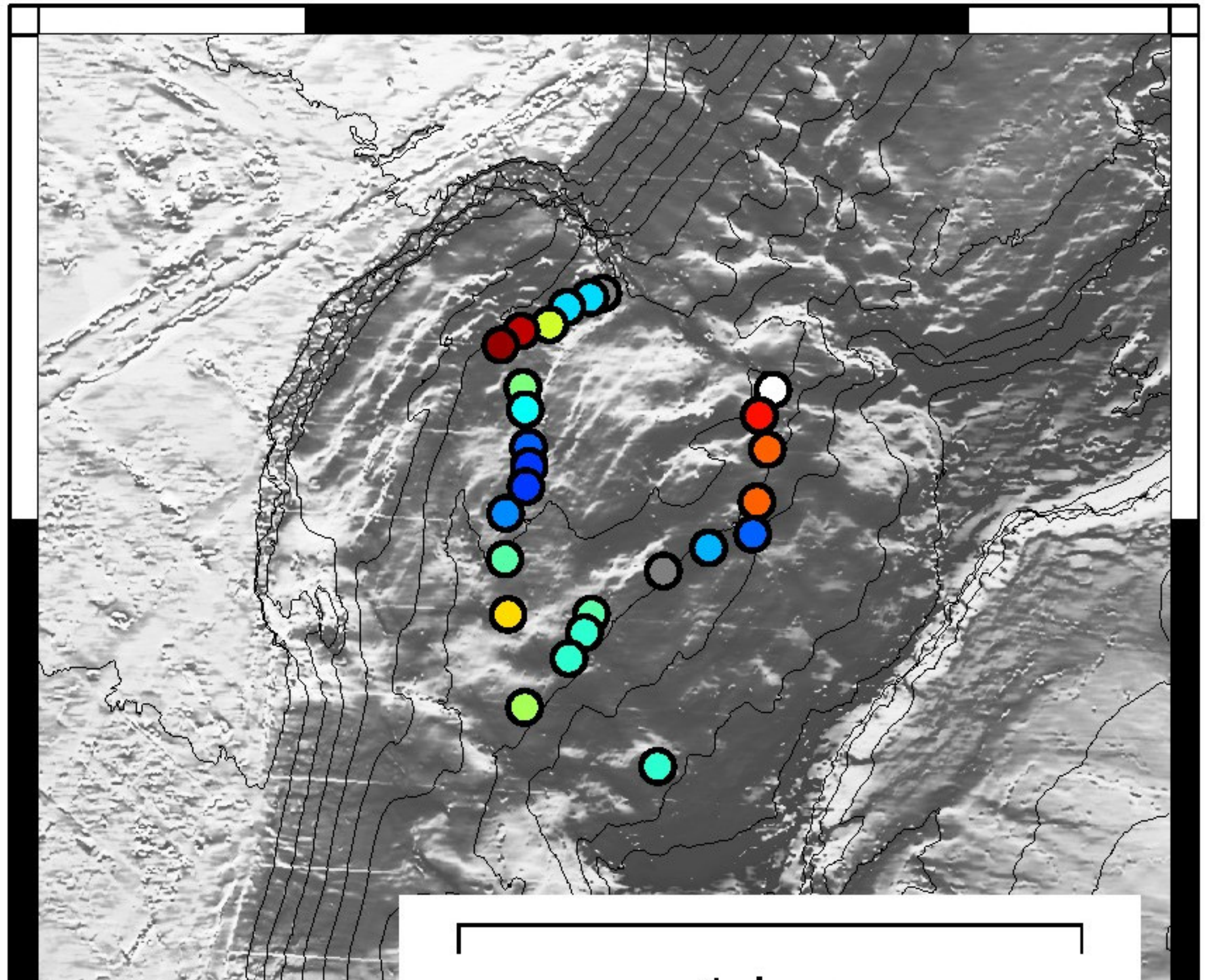
B



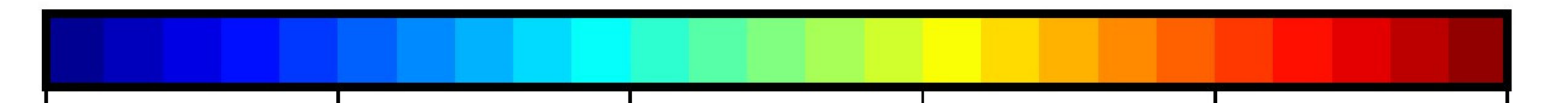
Accepted Article



Accepted Article

 $-72^{\circ}09'36''$ $-72^{\circ}09'00''$ $-16^{\circ}22'12''$

1 km

 $-72^{\circ}09'36''$ $-72^{\circ}09'00''$ 

0.0

0.5

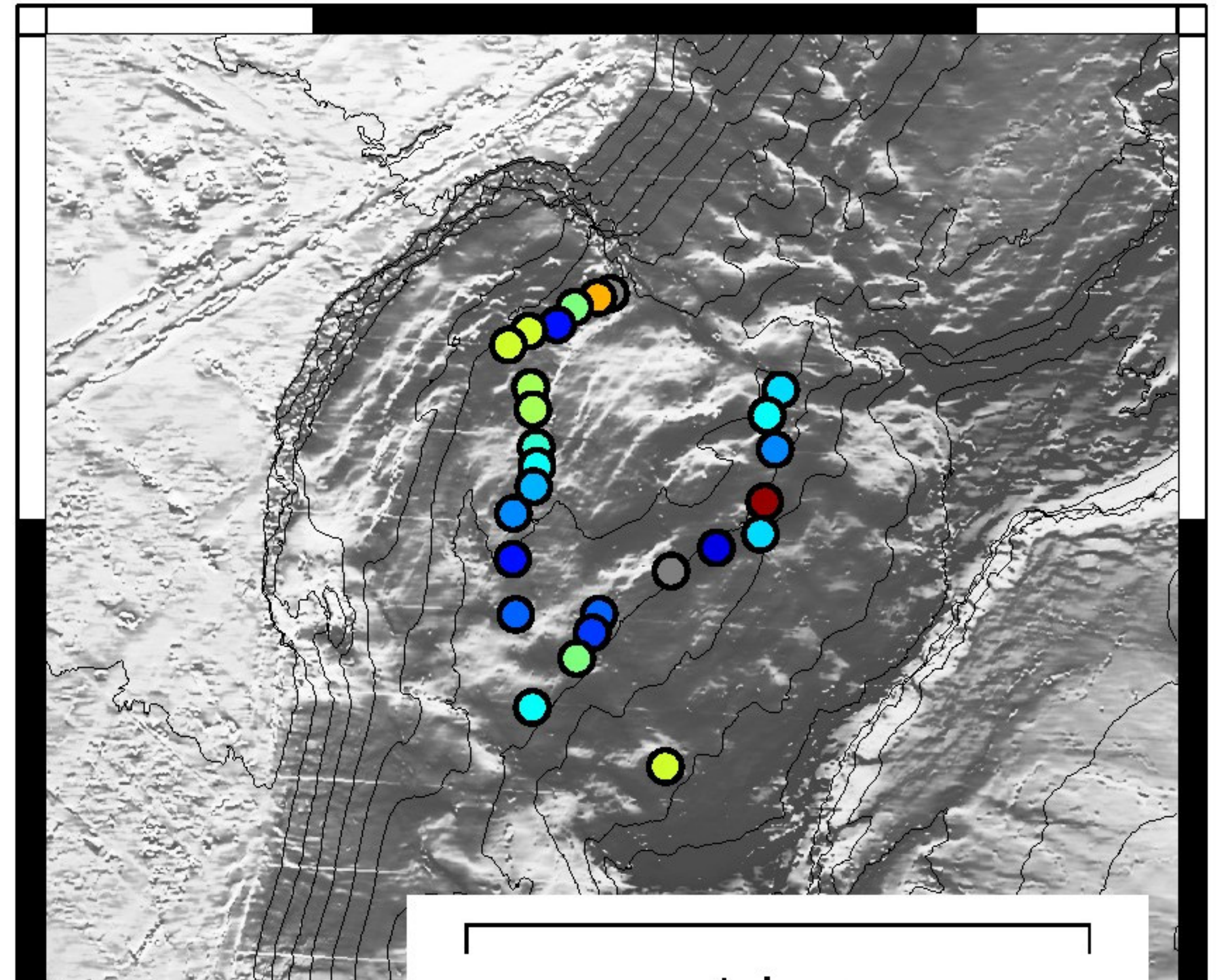
1.0

1.5

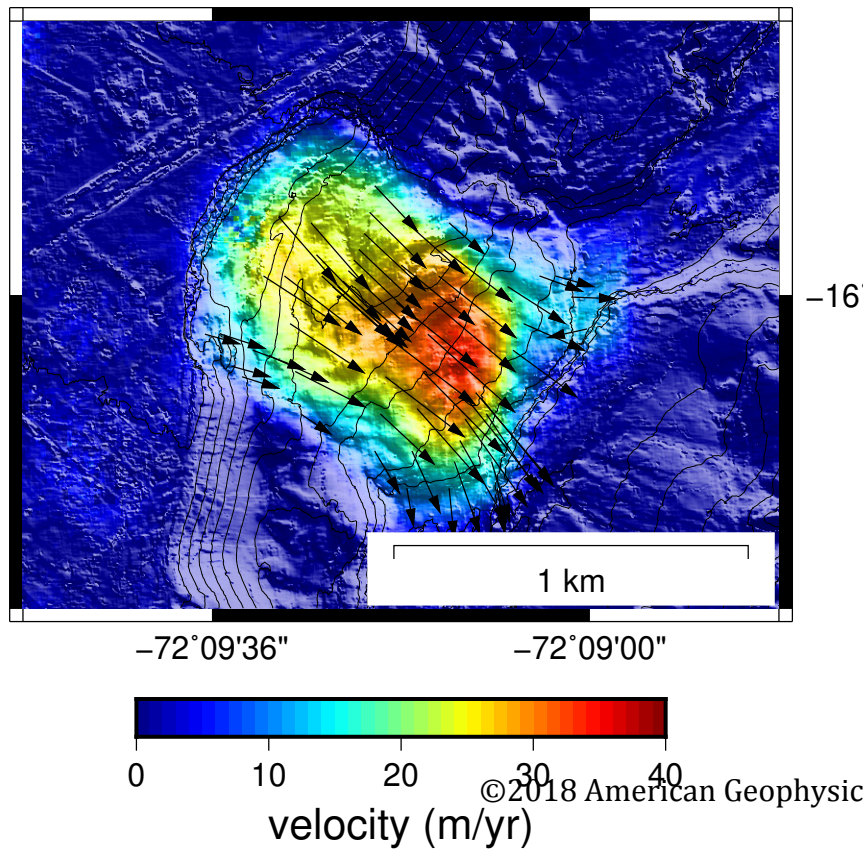
2.0

2.5

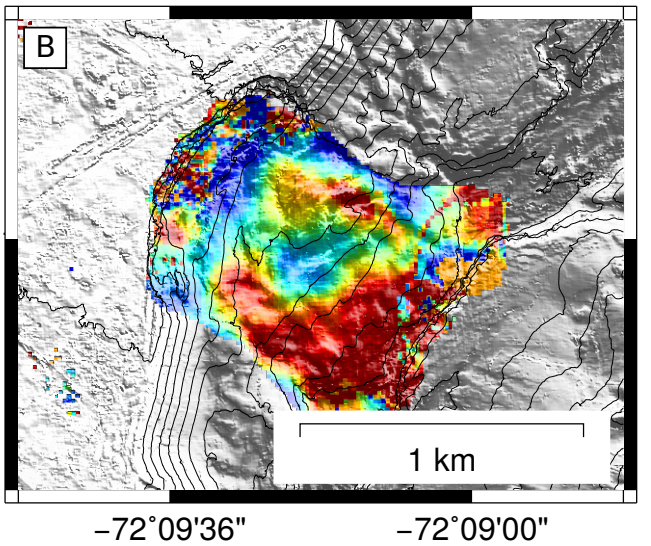
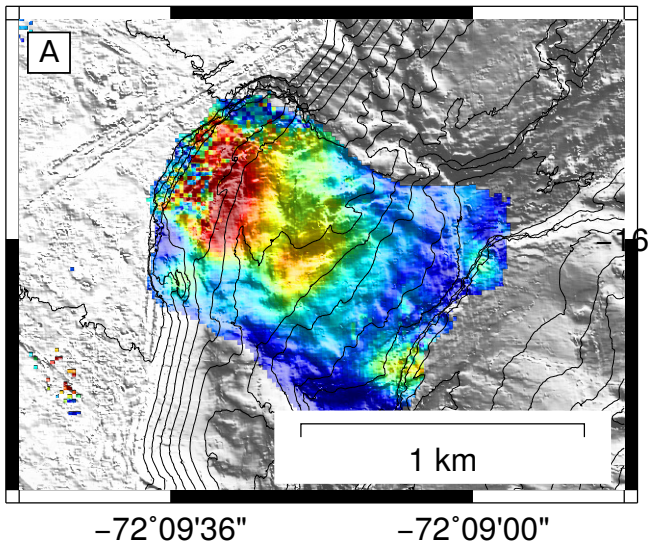
RMSE (m)

 $-72^{\circ}09'36''$ $-72^{\circ}09'00''$  $-72^{\circ}09'36''$ $-72^{\circ}09'00''$

Accepted Article



Accepted Article



Magnitude (m)

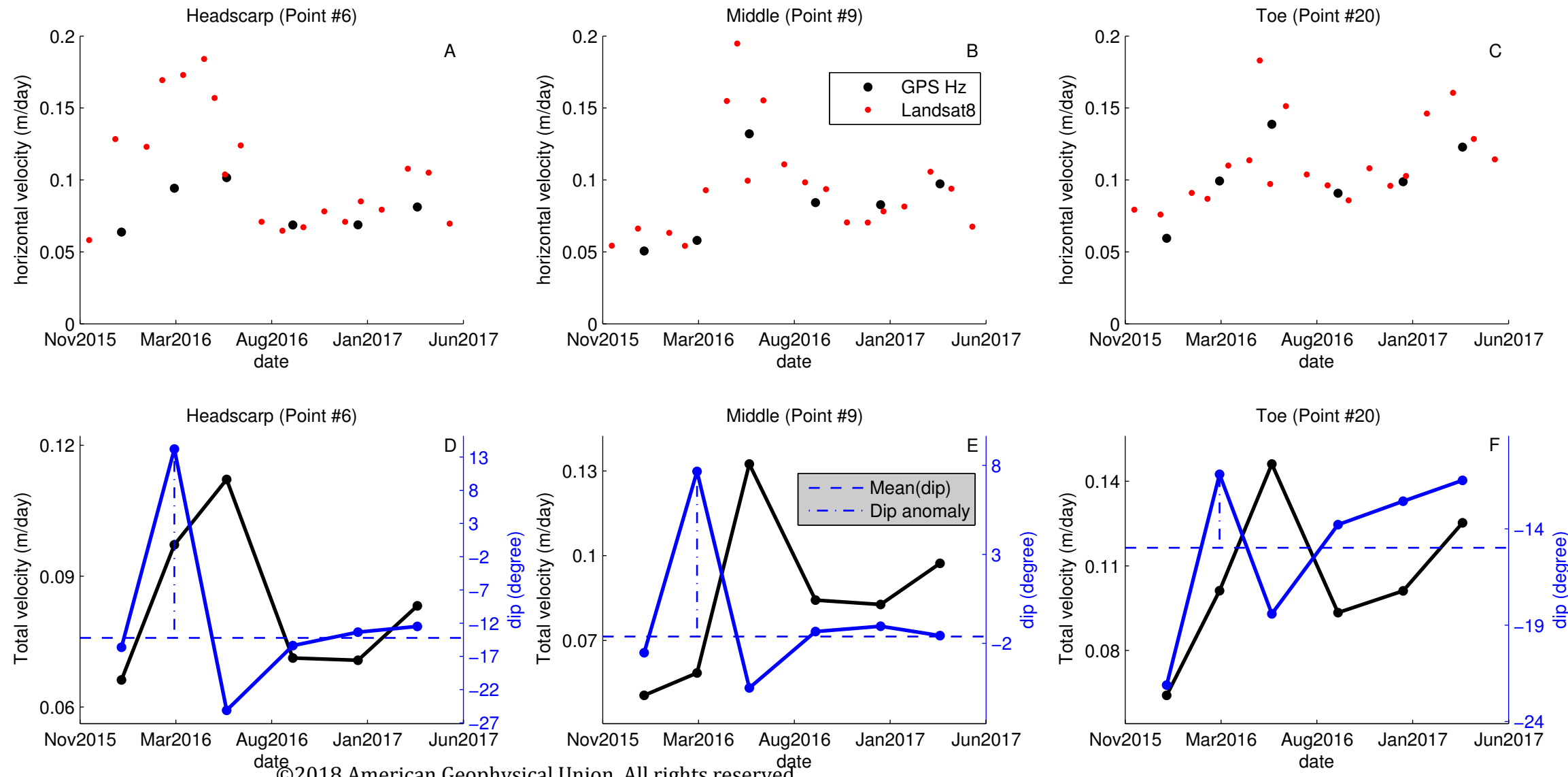
©2018

American Geophysical Union. All rights reserved.

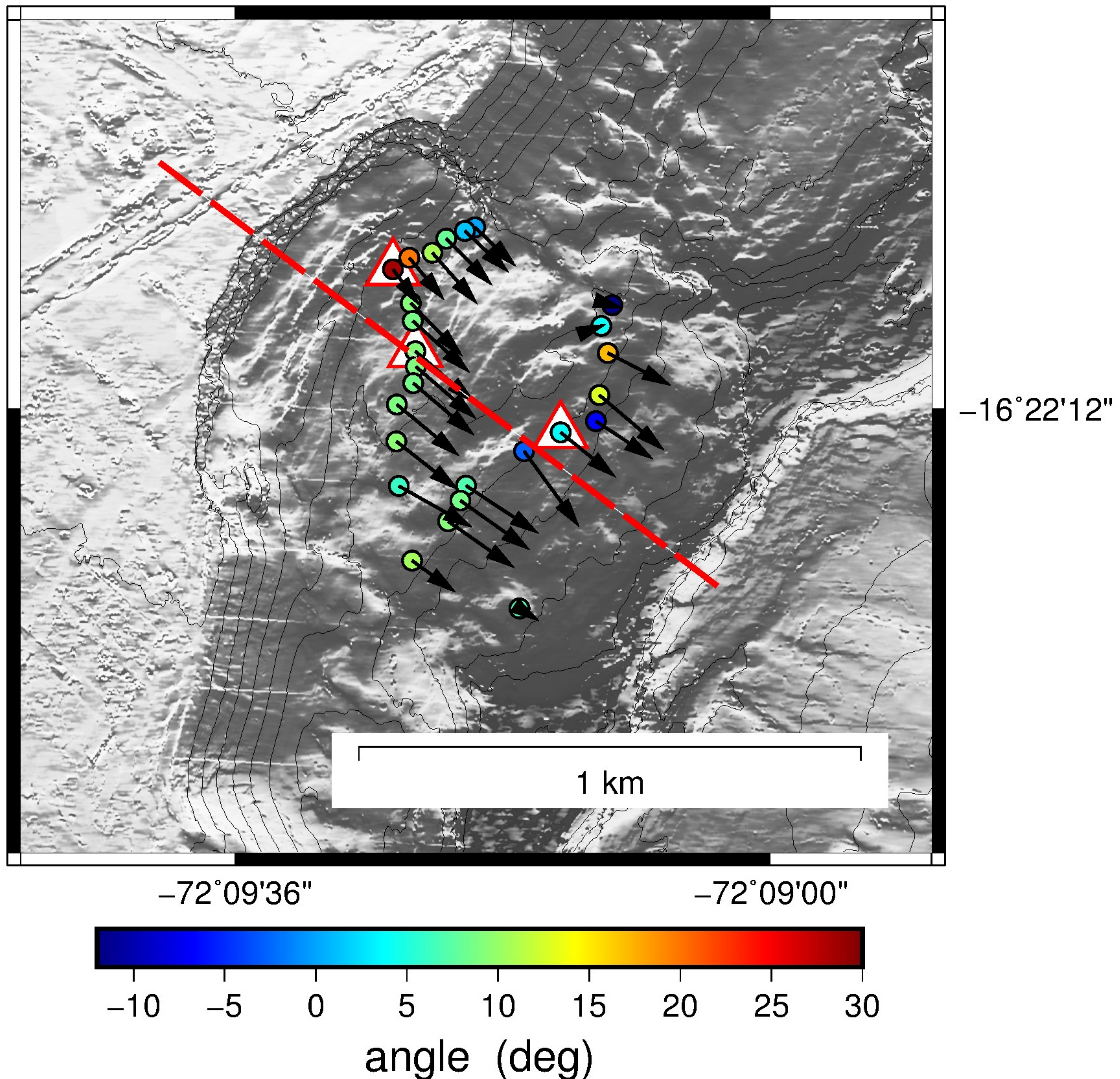


t0

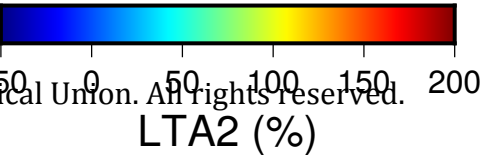
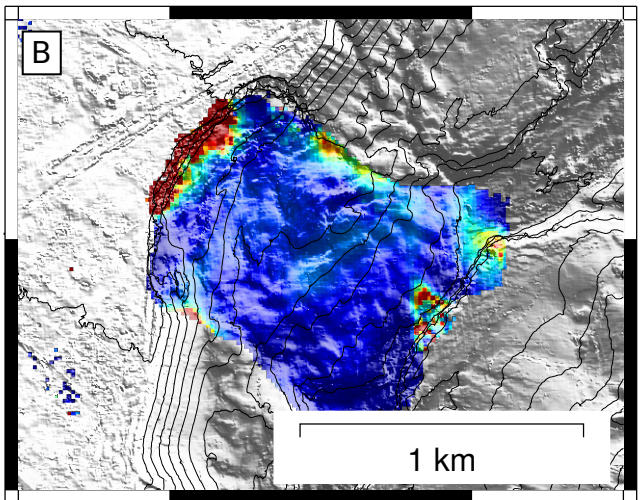
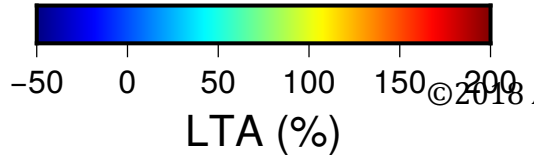
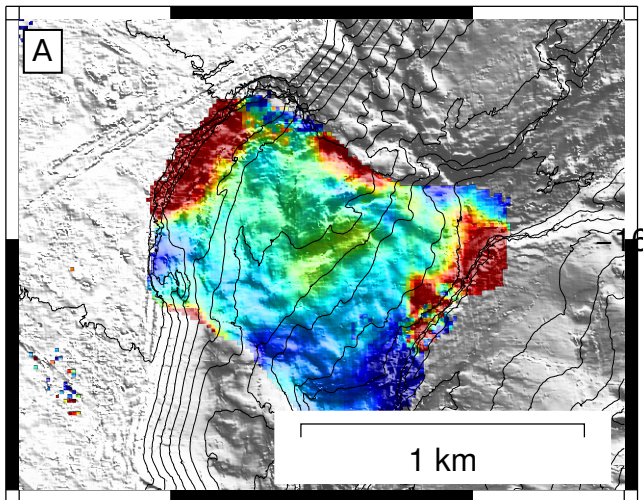
Accepted Article



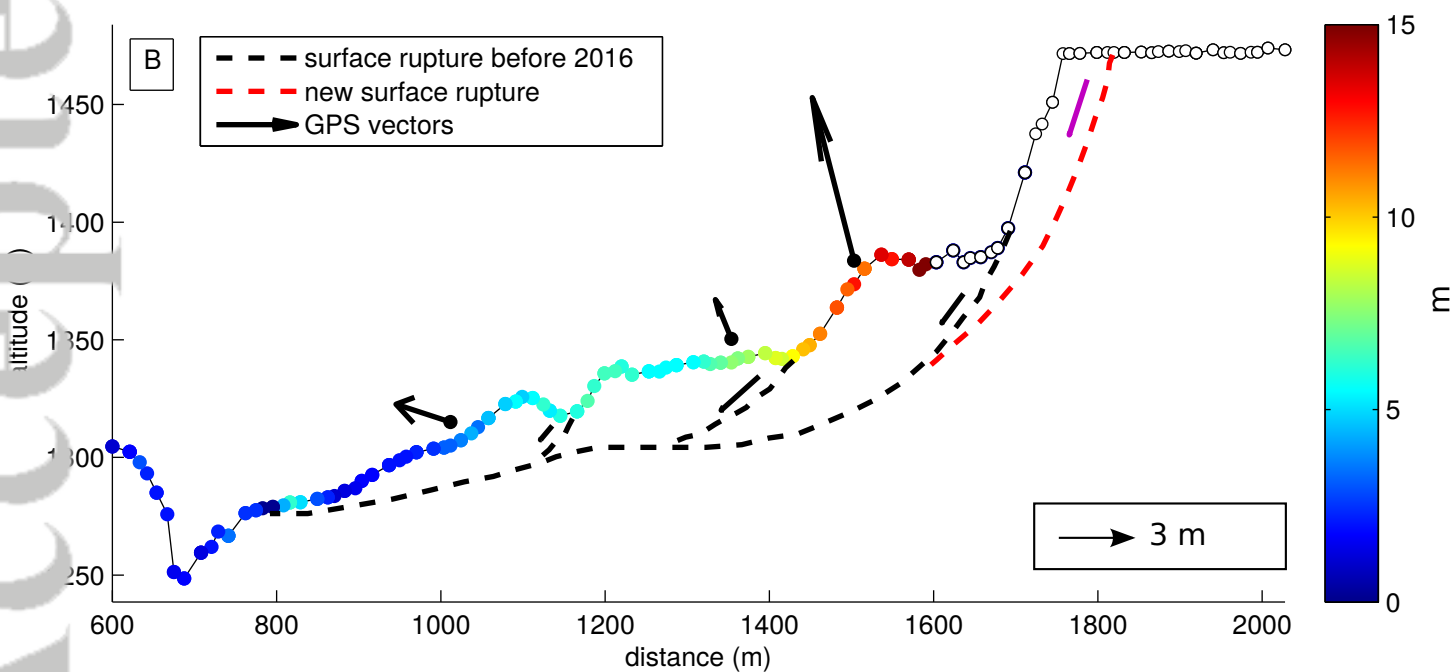
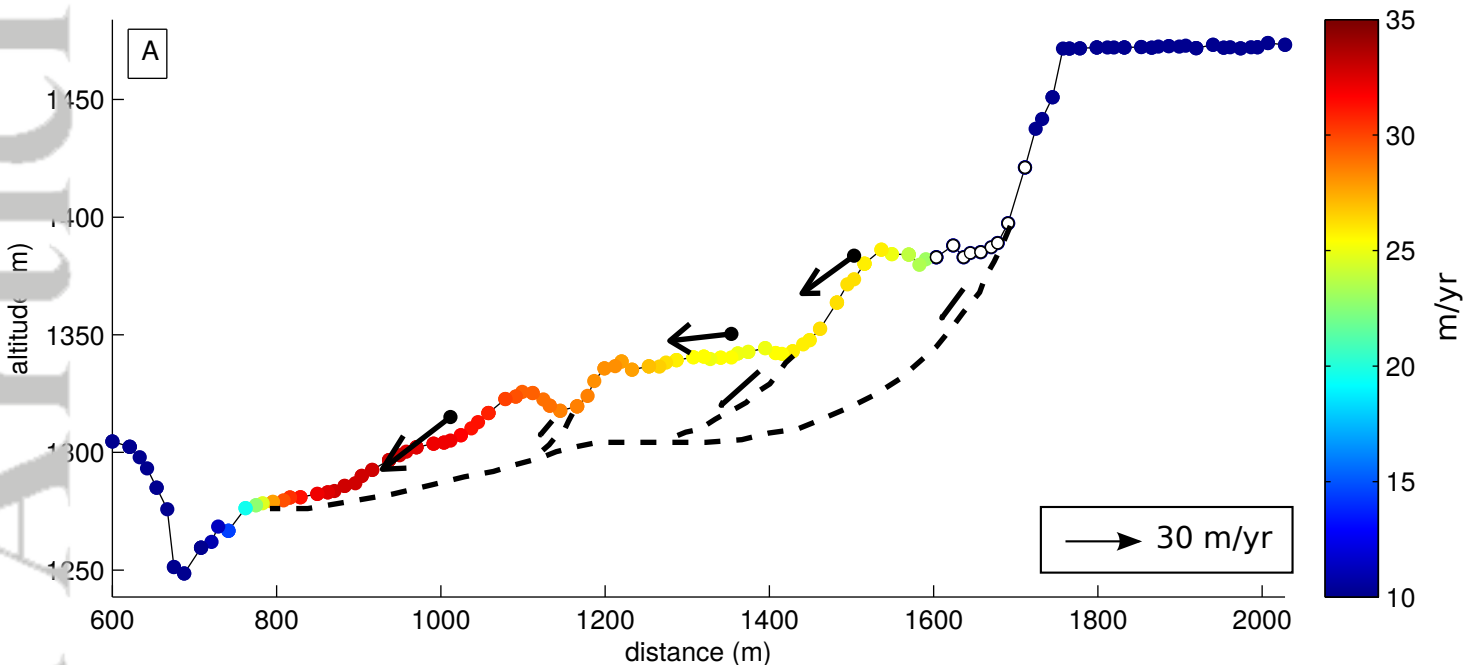
Accepted Article



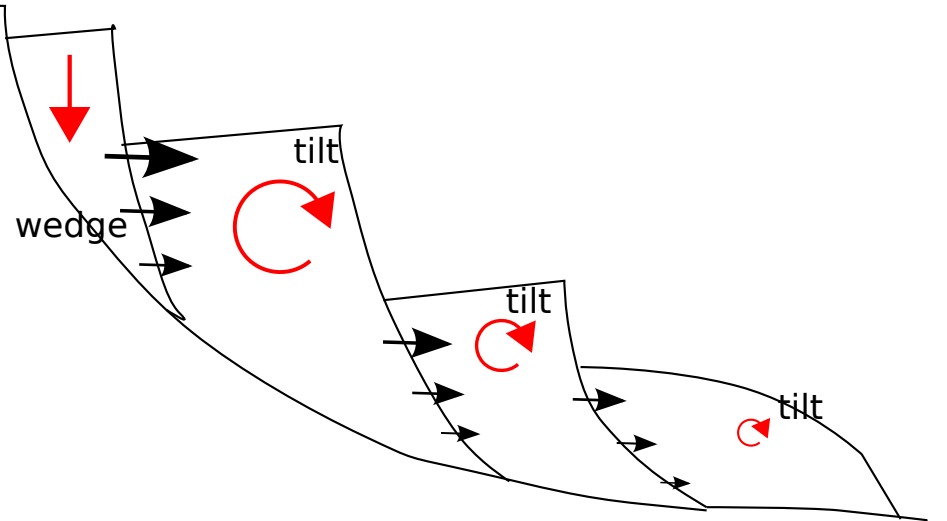
Accepted Article

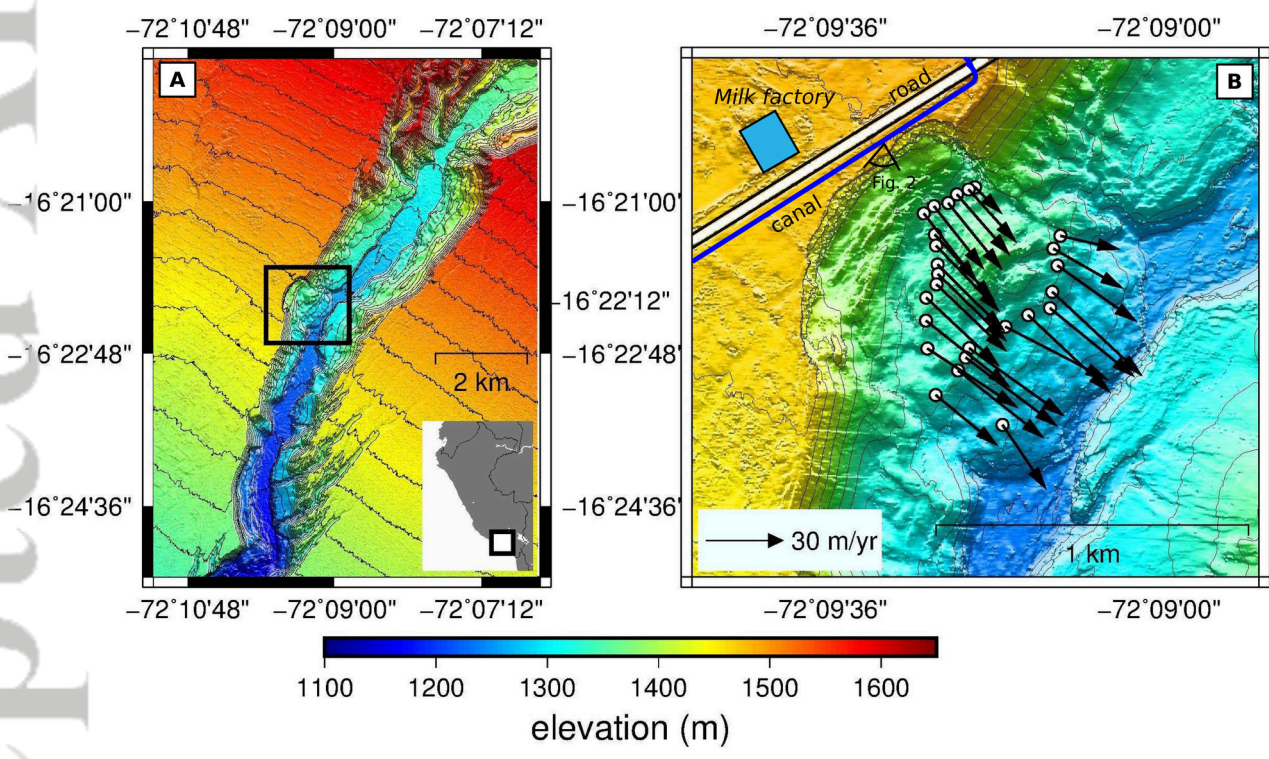


Accepted Article



Accepted Article



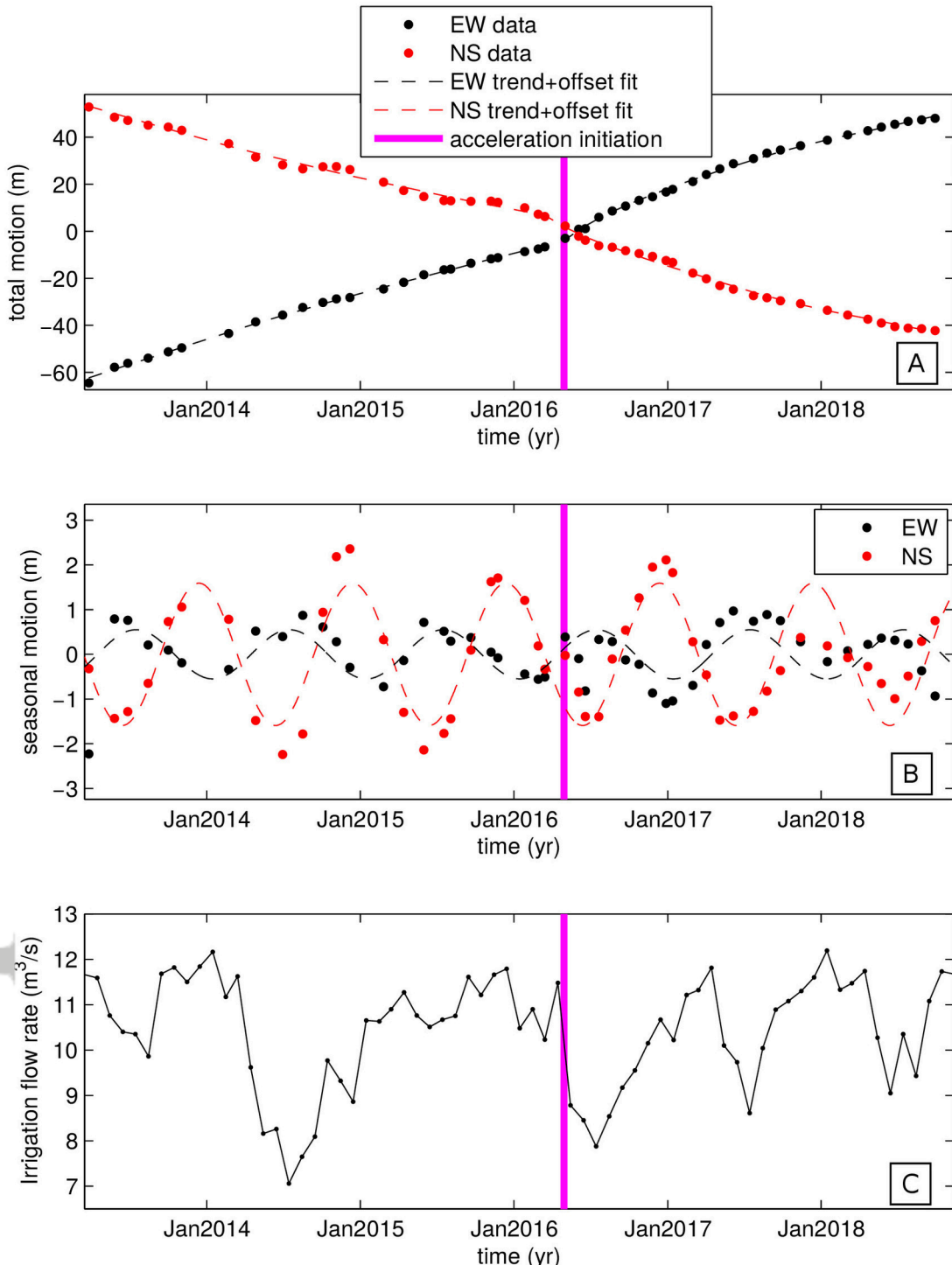


2018jf004920-f01-z-.eps

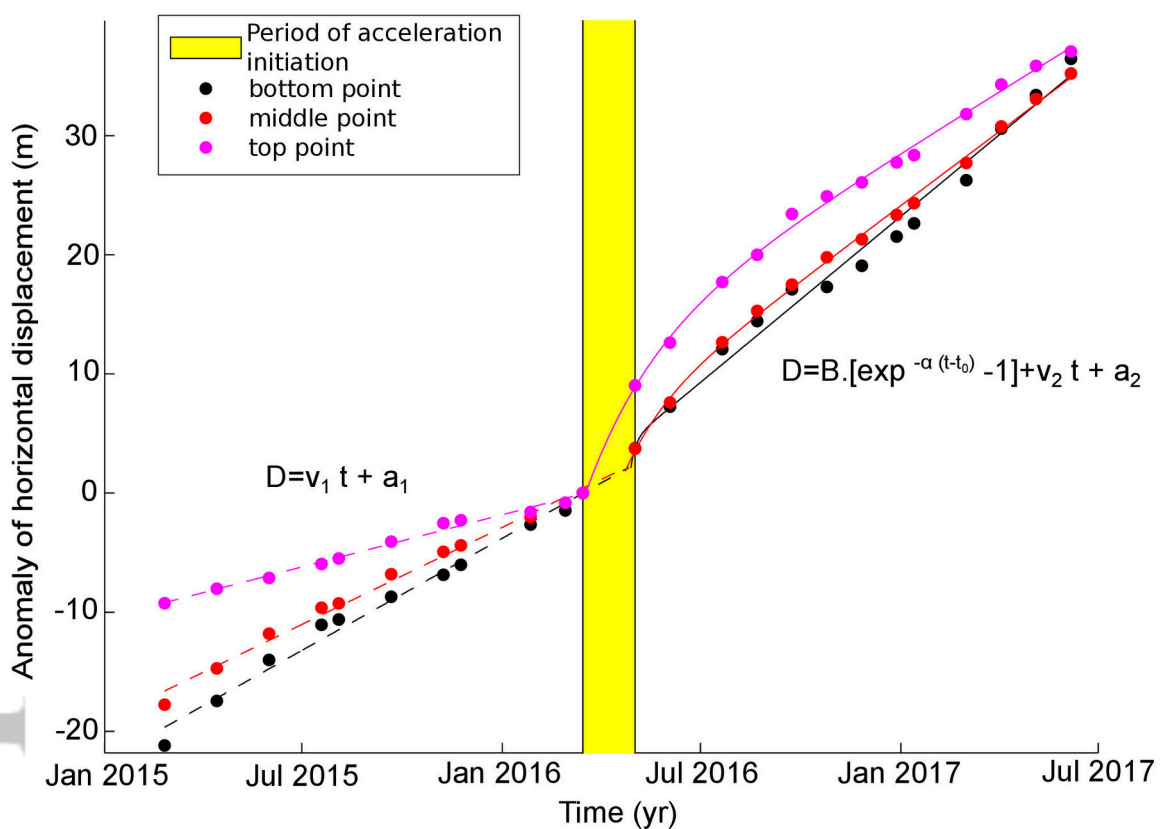
Accepted Article



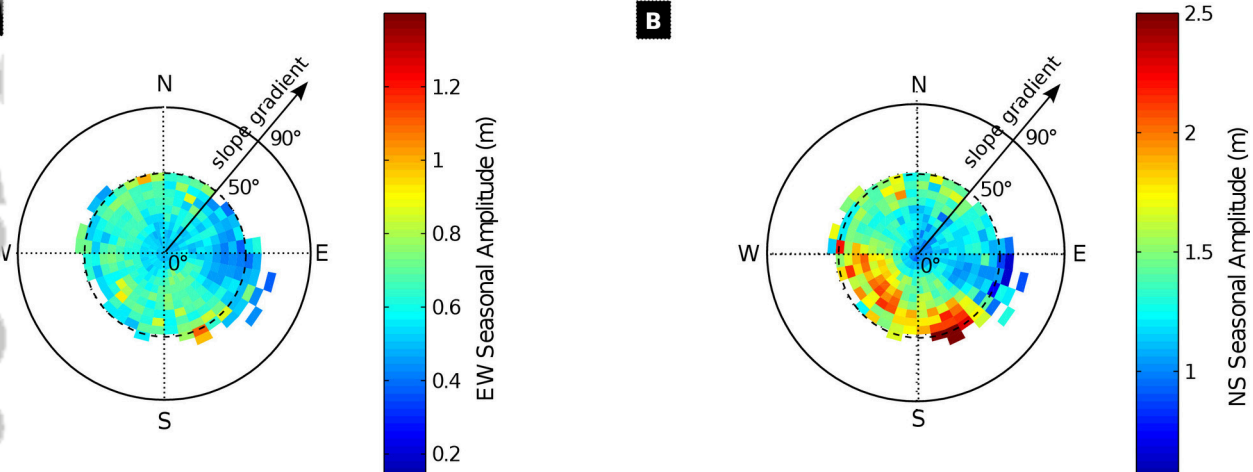
2018JF004920-f02-z-.jpg



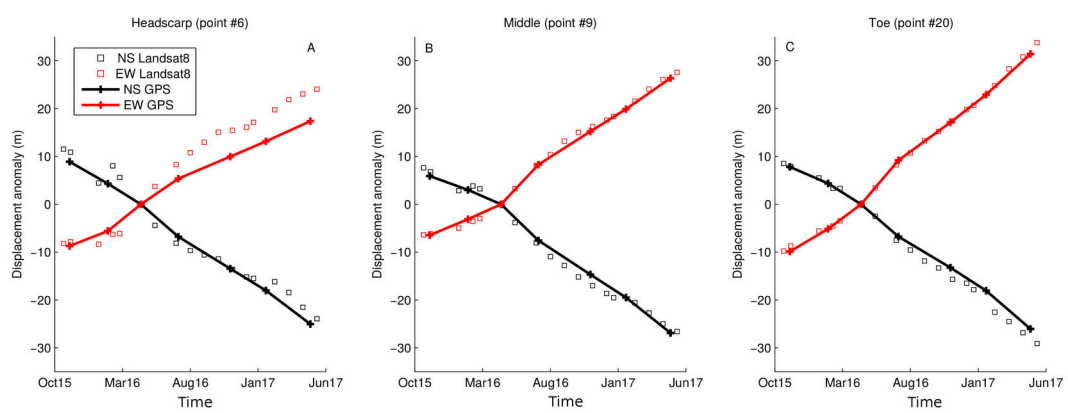
2018jf004920-f03-z-.eps



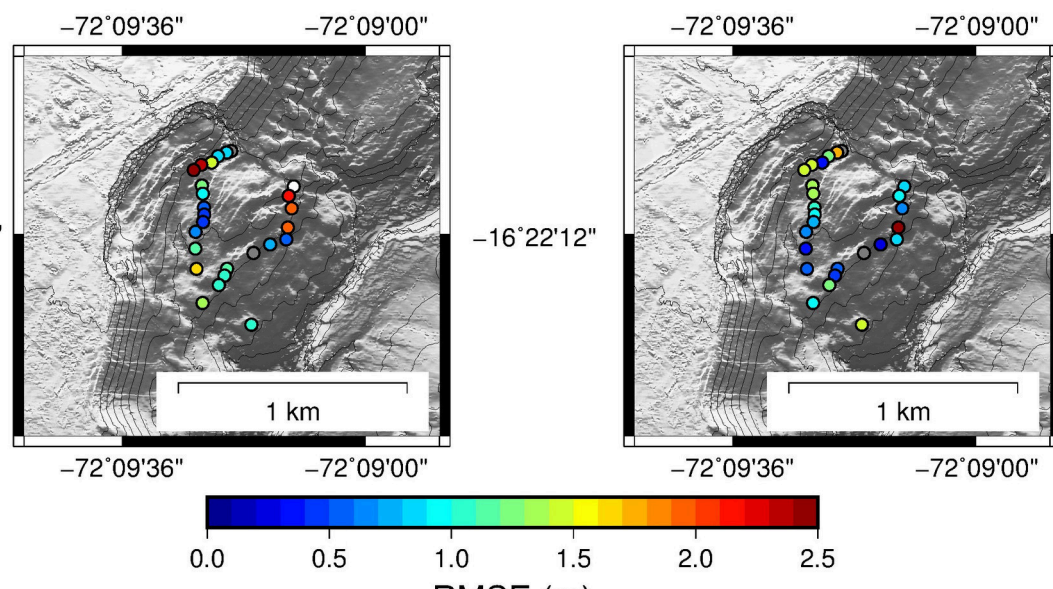
2018jf004920-f04-z-.eps



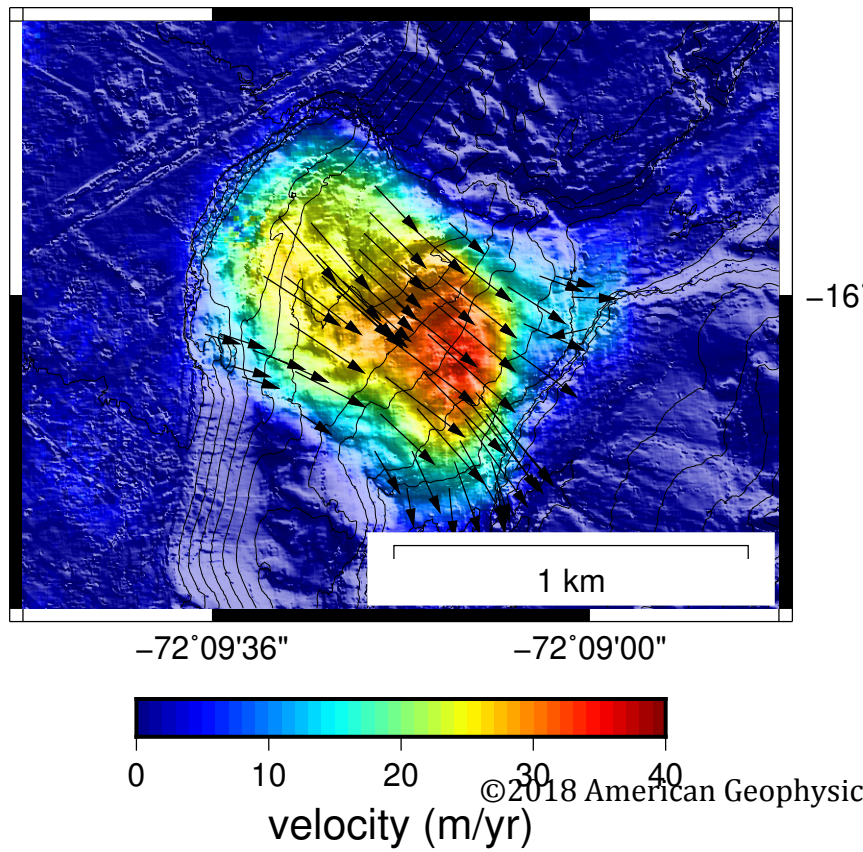
2018jf004920-f05-z-.eps

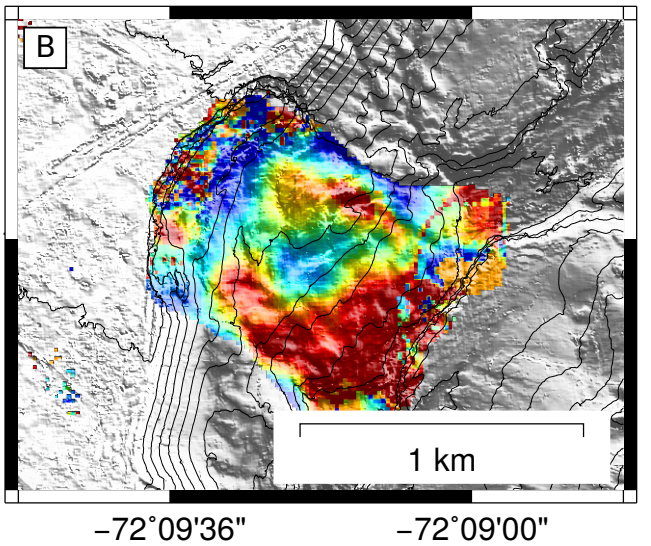
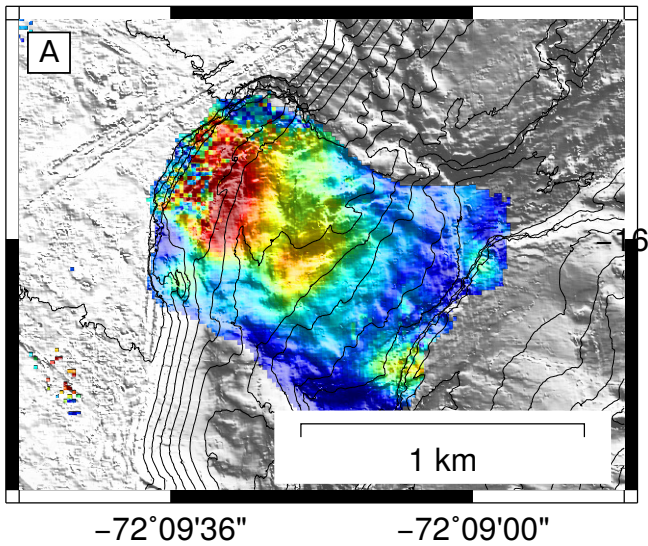


2018jf004920-f06-z-.eps



2018JF004920-f07-z-.jpg



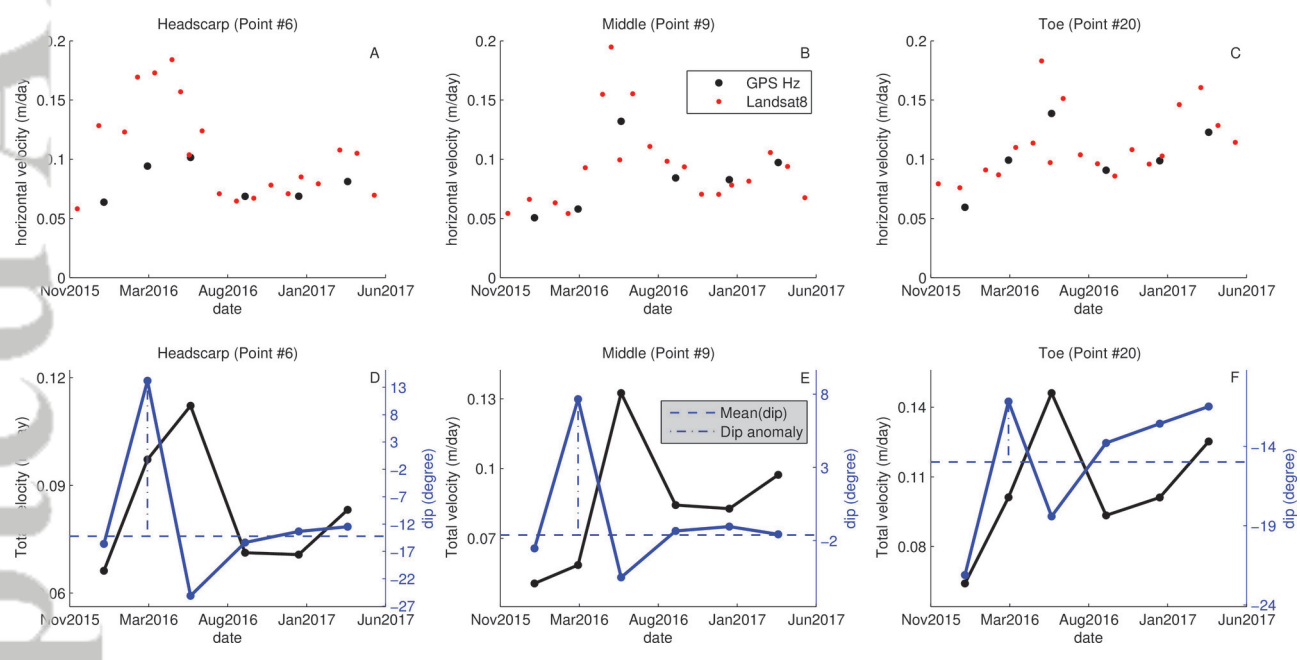


Magnitude (m)

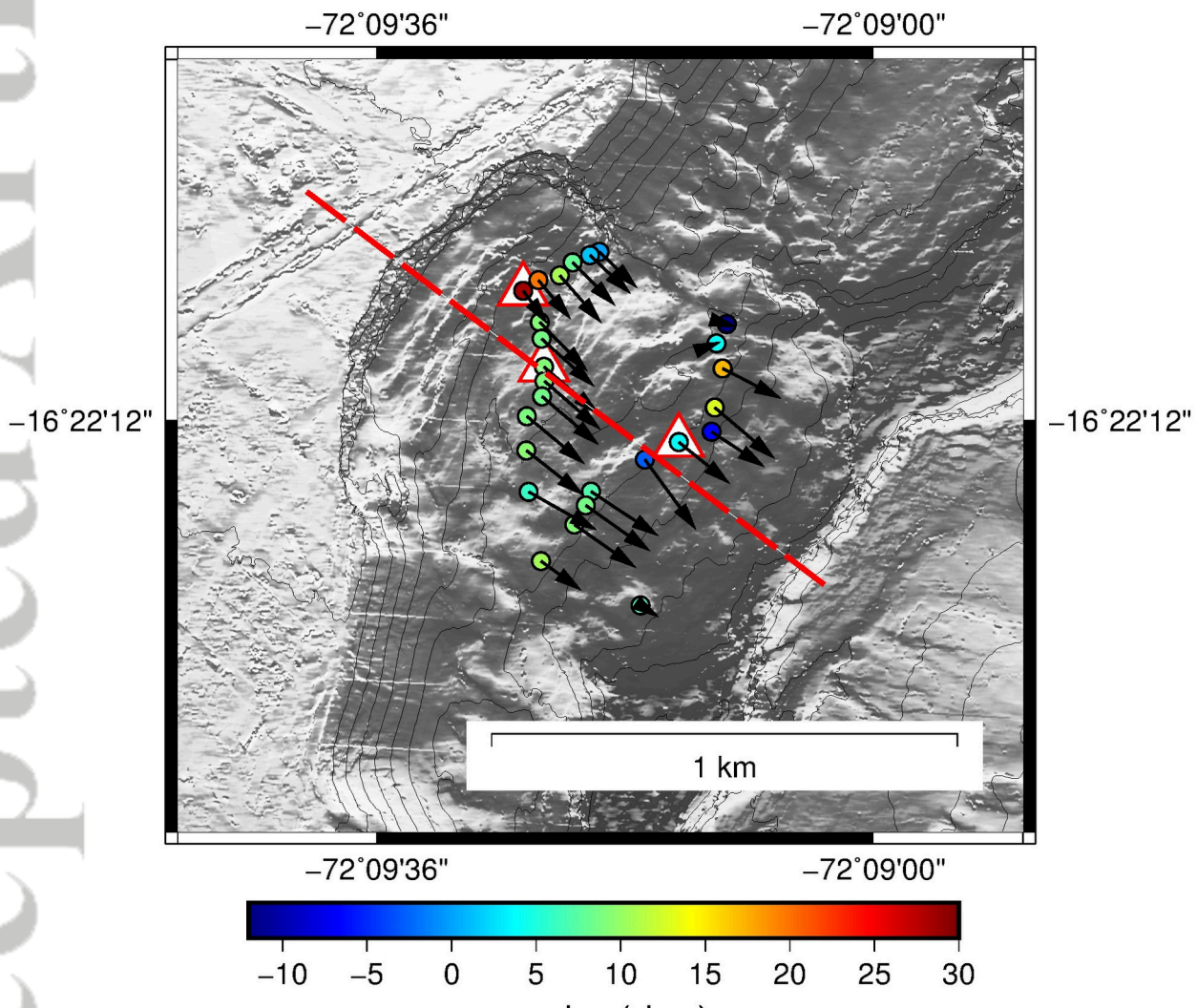
©2018 American Geophysical Union. All rights reserved.



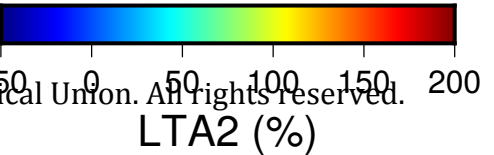
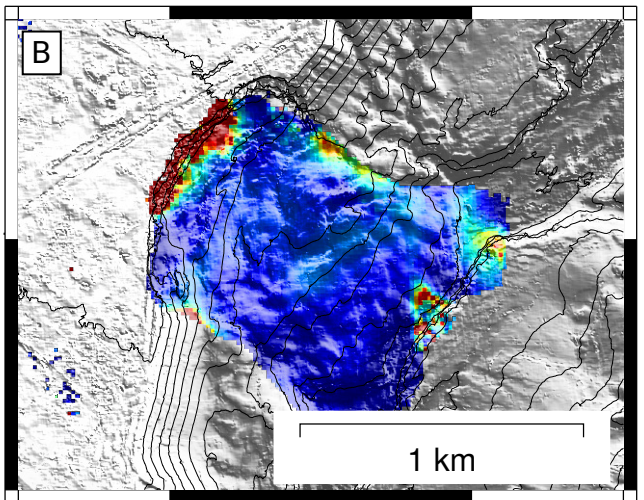
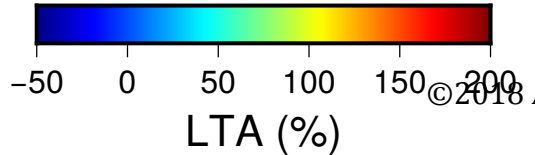
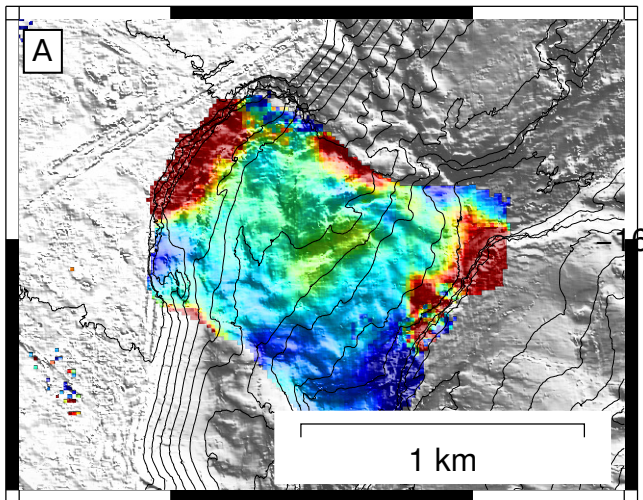
t0

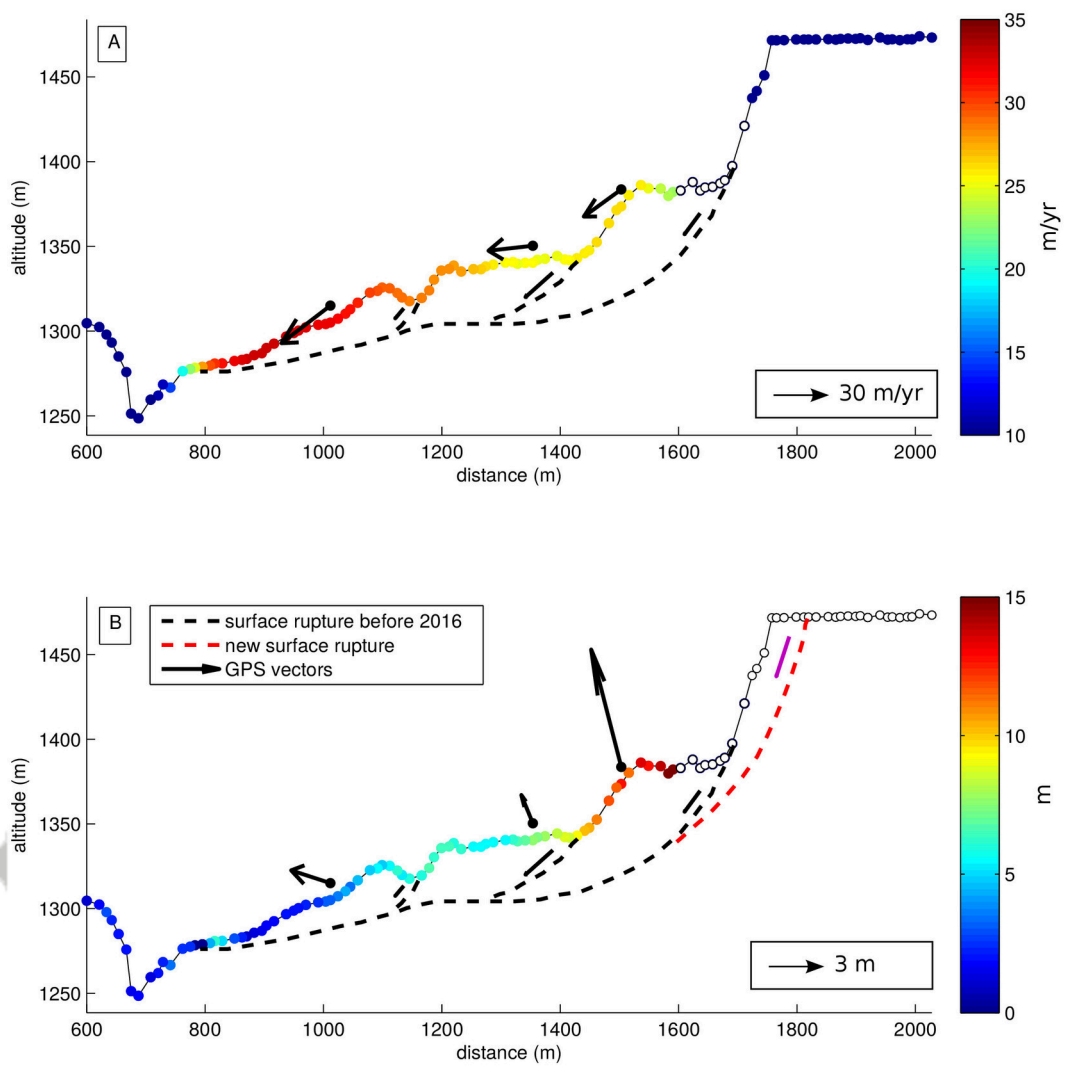


2018jf004920-f10-z-.eps

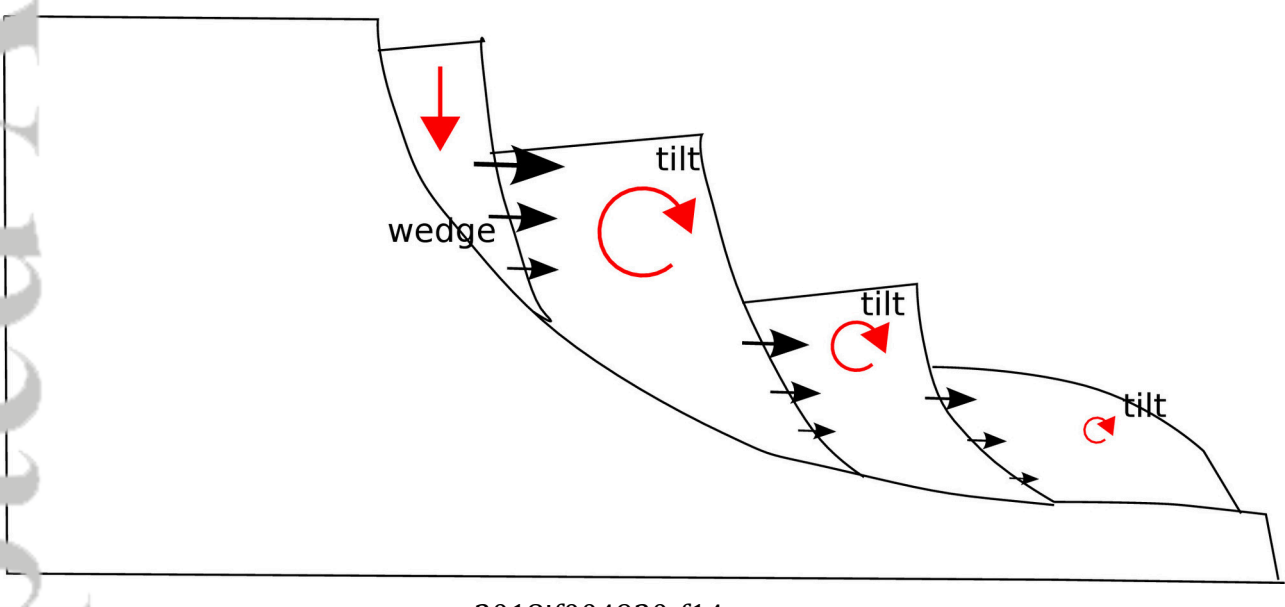


2018JF004920-f11-z-.jpg





2018jf004920-f13-z-.eps



2018jf004920-f14-z-.eps